University of Alberta

BUCKLING OF A THIN, VISCOUS FILM IN AN AXISYMMETRIC GEOMETRY

by

Sanjay Bhattacharya

A thesis submitted to the Faculty of Graduate Studies and Research
in partial fulfillment of the requirements for the degree of

Master of Science

Department of Mechanical Engineering

Spring 2013
Edmonton, Alberta

Abstract

An experimental study of the shear-induced buckling of a thin, viscous film in an axisymmetric geometry is presented. Rotating the inner boundary relative to a stationary outer one, generates large in-plane shear forces in the laterally constrained millimetric film, which leads to buckling of the viscous layer manifest as waves on the film surface. Regarding as independent variables the rotation rate, the gap width between the inner and outer boundaries and the film thickness and viscosity, the focus is on determining the number of waves excited plus their phase speed and amplitude by post-processing the experimental images in MATLAB. Experimental measurements of the number of waves excited, in the region between the onset of instability and the point of wave breaking, matches well with analogue predictions derived from an adaptation of the Foppl von Karman equation, which was originally developed to consider the wrinkling of an elastic membrane.

Acknowledgements

I would like to take this opportunity to express my gratitude towards all those who have helped me. First and foremost, I would like to thank Dr. Morris Flynn, the supervisor of my research program. He has been by my side at every stage and provided valuable ideas, suggestion and assistance throughout my research. I would also like to thank Dr. David Nobes for sharing optical equipment with our laboratory. Moreover, I wish to thank the technicians of the Department of Mechanical Engineering at the University of Alberta, who fabricated some of the experimental infrastructure that I used in my research. I must mention the names of Bernie Faulkner at the mechanical workshop for his assistance from time to time and Rick Conrad for electronics support. Lastly, I would like to thank my family and friends for always creating a positive environment that has helped me in my journey so far.

The funding for my research has been provided by the Department of Mechanical Engineering at the University of Alberta and NSERC through the Discovery Grant program.

Table of contents

List of tables

List of figures

List of symbols

A	Wave amplitude.
C_p	Phase speed of the waves.
D	Depth of lower fluid.
h	Film thickness.
H	Center-plane deflection of the film.
L	In-plane (horizontal) length scale, e.g. R_o.
m	Azimuthal wave number.
m^*	Azimuthal wave number of the most unstable mode.
$\mathbf{n}$	Unit normal vector.
P	Fluid pressure.
R_i	Inner radius (outer-most radius of disc assembly).
R_o	Outer radius (inner-most radius of glass beaker).
$\mathbf{T}$	Surface traction vector.
T	Characteristic time scale: $\sqrt{(R_o/g)}$.
t	Time.
$\boldsymbol{u}$	Velocity vector.
u, v and w	Radial, azimuthal and vertical components of velocity, respectively.
x, y, z, r and θ	Coordinate axes (directions).

β	Non-dimensional radius (R_i / R_o).
γ	Net surface tension.
γ^+ / γ^-	Surface tension of air-film and film-water interface.
ε	Non-dimensional film thickness (h / R_o).
Λ_1 and Λ_2	Constant coefficients as in equation 1.7.
μ	Dynamic viscosity.
ν	Kinematic viscosity.
ρ	Density of film.
ρ^-	Density of lower fluid.
σ	Growth rate of perturbation.
τ	Shear stress.
Υ_1 and Υ_2	Non-dimensional terms incorporating gravity and surface tension respectively as in equation 1.11.
Ω	Angular speed (of disc assembly).
∇	Gradient operator.

Chapter 1 - Introduction

1.1 Overview

Low Reynolds number viscous flows are slow-moving flows where inertial effects can be neglected. Due to shear, the phenomenon of buckling or wrinkling is often observed in free surface flows of low Reynolds number fluids. Instances of such flows can be found in natural as well as man-made situations. A common example that can be seen in everyday life is that of syrup being poured on a plate. As the syrup piles up, buckling is observed. Likewise with batter poured into a pan or paint poured into a tray. Whereas the previous examples consider the buckling of a vertical filament of viscous fluid, similar behavior can also be observed in flows that are primarily horizontal. For example, Griffiths (2000) describes a lava flow as a gravity current of molten rock that may flow at low to moderate Reynolds number. The molten material coming out of the Earth's crust due to an effusive or non-explosive eruption is composed of silicate liquids, crystals and gas bubbles, and is therefore a highly viscous fluid that often moves at relatively slow speeds. This viscous flow may be channelized, whereby it is steered by topography, which gives rise to a velocity gradient in the horizontal and/or vertical plane as shown in figure 1.1. The velocity gradients, in turn, generate shear. The top surface, being exposed to the atmosphere, cools down relatively quickly and solidifies forming a thin crust. As noted by Slim et al. (2009), the molten lava flowing underneath exerts a drag on this solidifying layer and causes buckling as shown schematically in figure 1.2.

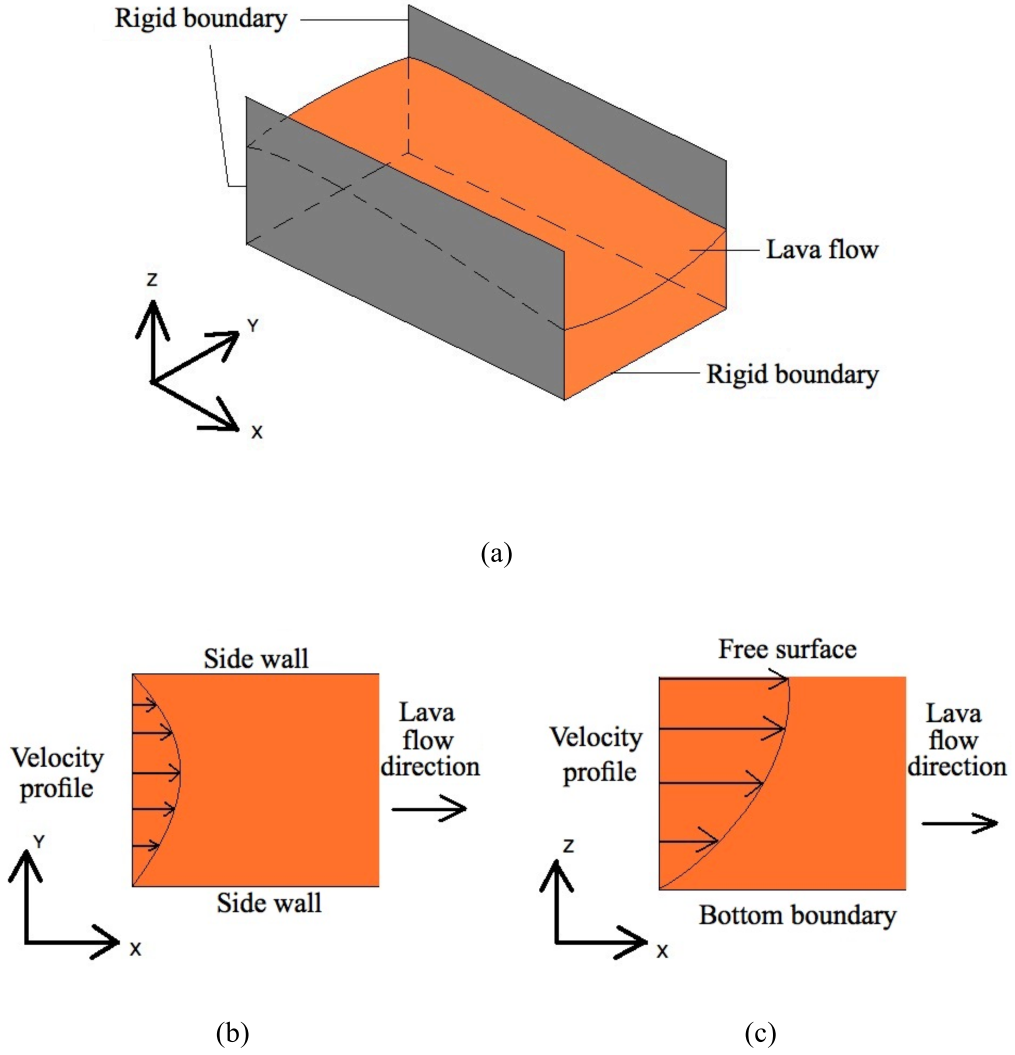

Figure 1.1: Channelized lava flow as an example of a low Reynolds number viscous flow (a) bounded by rigid surfaces at the bottom and along the sides, (b) top view showing the velocity profile along a horizontal plane and (c) side view showing the velocity profile along a vertical plane.

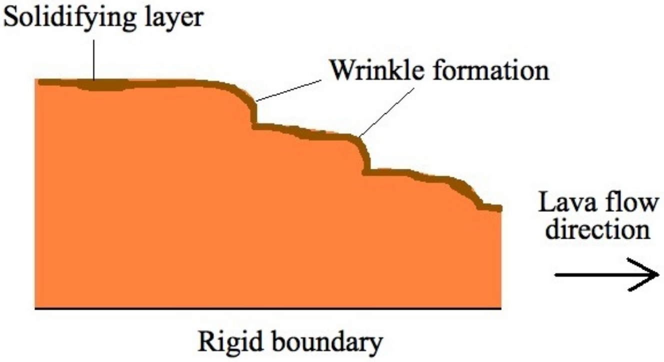

Figure 1.2: Wrinkling of the surface layer due to shear.

Viscous flows may alternatively propagate along a fluidic rather than a solid boundary. An infamous, if unfortunate, natural example is that of a marine oil spill in which case the wind exerts a shear stress on the top of the oil layer. Light winds may lead to wrinkle formation, i.e. out-of-plane displacements in the form of waves. Conversely, strong winds may lead to film rupture, exposing the water below. A ruptured film spreads over a broader expanse when compared to a continuous oil slick as noted by Dave (2011). The type of remediation response is determined by the movement of the slick and also by the nature of the oil due to weathering. For example, if the slick has spread over large distances and has been broken into small fragments or 'tar balls', oil recovery via skimming operations can remove only a fraction of the spilled oil (ITOPF 2012). Film rupture also has an important impact on waterfowl and marine life as we illustrate schematically in figure 1.3. In panel (a), a continuous layer of oil makes it impossible for birds to avoid contact with the oil, which may damage their feathers and lead to hypothermia (Kerly 2005). When the oil film is ruptured, by contrast, birds may find patches of open water, thereby lowering the chances of coming into contact with the spilt oil (figure 1.3b).

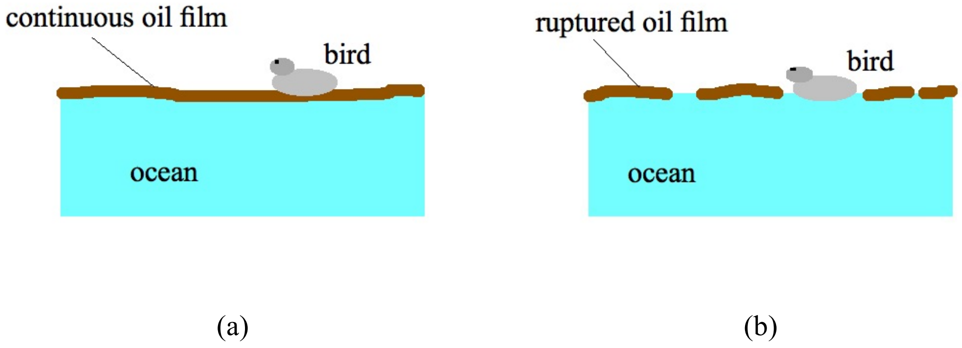

(a) (b)

Figure 1.3: (a) Continuous oil film and (b) ruptured oil film.

The above comments are especially significant in light of the 2010 Deepwater Horizon oil spill, which, according to Chakrabarty et al. (2012), represents the largest accidental marine oil spill to date and required approximately three months to bring under control. As noted out by Fisher (2010), up to 79% of the spilt oil could not be recovered by conventional methods such as burning or skimming. Whether by conventional or unconventional means, it is very likely that more of the oil could have been recovered if there was a better understanding of the rheology of the oil film related to the action of waves and wind shear, film rupture and the formation of tar balls. Thus, it is important to understand the shear conditions under which such rupture might take place in a thin layer of viscous fluid. Even more generally, it is of interest to relate out-of-plane deformations of a viscous film to the associated shear forces. Such is the focus of the present thesis.

The examples listed above admit complicated dynamics in which surface buckling arises due to shear forces, which are in turn related to gradients of velocity or viscosity. Herein, we restrict our attention to thin layers of viscous liquids, i.e. films that are thin in the sense that their thickness is much less than an associated characteristic horizontal length scale. We also focus on films having traction boundary conditions along their upper and lower surfaces. By investigating the out-of-plane deformation of such films, we may simultaneously draw inferences regarding the buckling of a thin elastic membrane as studied for instance by Southwell and Skan (1924); in examining, theoretically, the deformation of thin plates such as girders, they studied the effect of uniform in-plane shear on buckling behavior. This association relies upon the Stokes-Rayleigh analogy, by which the behavior of a linear elastic solid is analogous to that of a Newtonian viscous liquid albeit with some differences. As an example and as noted by Teichman (2002), Lord Rayleigh (1945) showed that the volumetric energy dissipation rate in the case of fluids differs from its elastic analogue by a time derivative. Although Lord Rayleigh's analogy focuses upon bulk behavior, it should be possible to extend similar ideas to thin films with suitable modifications. For example, when compared to a bulk medium, free surfaces must be considered. Consequently surface tension forces must be incorporated, at least in the fluidic problem. The veracity of the Stokes-Rayleigh analogy as applied to a slender geometry is reflected in the similarity of wrinkle patterns observed between an elastic membrane and a viscous film. To make the analogy quantitatively robust, strain in the case of the elastic membrane problem must be replaced with a strain rate in the viscous film problem (Teichman 2002). Likewise we must replace displacement and bulk modulus in the case of an elastic medium with velocity and dynamic viscosity, respectively, for a viscous liquid.

1.2 Theoretical considerations

A qualitative discussion of the Stokes-Rayleigh analogy was presented in the previous section. This section is dedicated to a greater understanding of the theoretical aspects underlying the buckling of a viscous film wherein quantitative details are presented. Building upon the Stokes-Rayleigh analogy, the Foppl von Karman equation, which was originally developed to study the buckling of elastic membranes, is reformulated so it may investigate the behavior of viscous films subjected to shear. Our discussion follows that of Teichman (2002) wherein similar topics are investigated.

We focus on the buckling of a thin, viscous film that is laterally constrained in an axisymmetric geometry, due to in-plane shear. Referring to figure 1.4 and relative to a fixed outer boundary, the rotation of the inner boundary leads to in-plane stresses that drive an out-of-plane displacement, H, of the film. Note that H is a function of r, θ and t, and can be a positive or negative quantity.

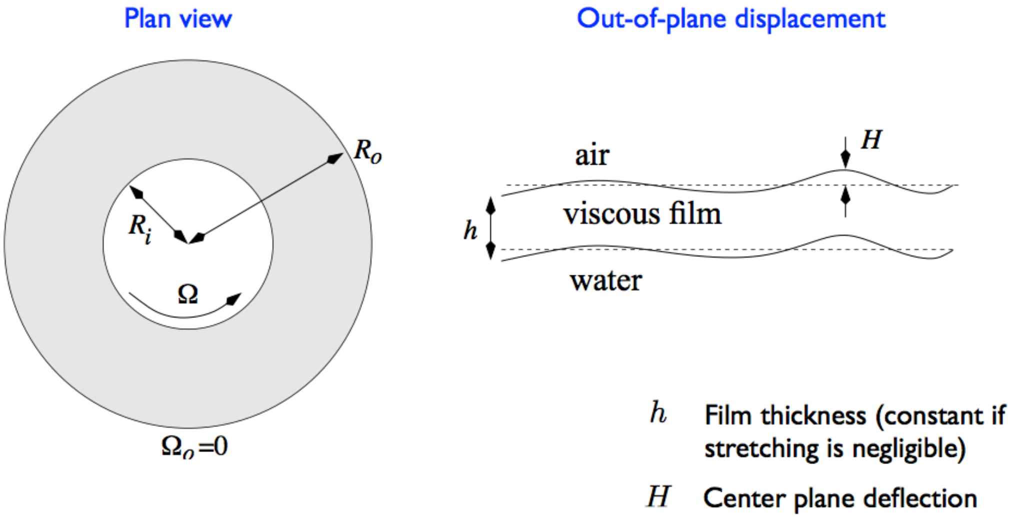

Figure 1.4: Out-of-plane displacements of a viscous film subjected to shear in an axisymmetric geometry.

The mass continuity equation for an incompressible flow is,

$$\nabla.\boldsymbol{u} = 0, \tag{1.1}$$

where $\boldsymbol{u}$ is the velocity vector. The momentum balance equation reads

$$\nabla P = \mu \nabla^2 \boldsymbol{u}, \tag{1.2}$$

where P and μ are the fluid pressure and dynamic viscosity, respectively. Here, inertial and centrifugal effects are neglected owing to the low Reynolds number. Note that these governing equations are applicable to a control volume that encompasses the entire volume of the film, limited by concentric boundaries on either side, the air above and the water below.

The above governing equations are subject to the following boundary conditions:

(i) Kinematic $$[w]_{z=H\pm h/2} = \frac{D}{Dt}\left(H \pm \frac{h}{2}\right), \tag{1.3}$$

where w is the vertical component of velocity, $z = 0$ coincides with the center plane of the undisturbed film and h is the film thickness.

(ii) Dynamic $$\sigma.\mathbf{n} = \mathbf{T}, \tag{1.4}$$

where **n** is the unit normal to the film surface and **T** is the surface traction which includes the effects of surface tension. The stress tensor σ is defined as

$$\sigma = -PI + \mu\,(\nabla \boldsymbol{u}^{\mathrm{T}} + \nabla \boldsymbol{u}\,) \tag{1.5}$$

in which I denotes the identity matrix and the superscript T denotes a matrix transpose.

Although the dynamic boundary condition (1.4) applies to both the 'Upper' and 'Lower' boundaries (figure 1.5), the parameters involved are different; namely, the surface tension values are different for the two interfaces and the density of the lower fluid, ρ^-, implicitly included in the pressure term, applies only to the 'Lower' boundary. With reference to figure 1.5, the boundary conditions applicable to the present geometry are summarized in table 1.1.

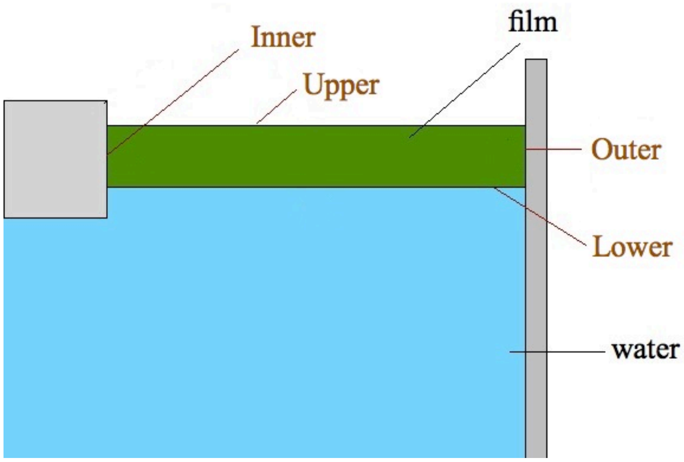

Figure 1.5: The boundaries of the film.

Table 1.1: Boundary conditions; note that u, v and w represent the radial, azimuthal and vertical components of velocity.

Boundary	Interface	Boundary conditions
Inner	film – (rotating) solid $r = R_i$	No slip: $v = R_i\Omega,\ w = 0$ No penetration: $u = 0$
Outer	film – (stationary) solid $r = R_o$	No slip: $v = 0,\ w = 0$ No penetration: $u = 0$
Upper	film – air $z = H+h/2$	$\frac{dv}{dy} = 0$ Kinematic (1.3) Dynamic (1.4)
Lower	film – water $z = H-h/2$	$\frac{dv}{dy} = 0$ Kinematic (1.3) Dynamic (1.4)

For the present research, where we are specifically interested in the pattern of free-surface waves that arises due to planar shear, the fluidic version of the Foppl von Karman equation is adapted to describe the out-of-plane motion. The Foppl von Karman equation originates from the full Stokes equations (1.1) and (1.2). However, a slender geometry approximation is made, which reduces the complexity of the governing equations. This slender geometry approximation requires that $H/L << 1$ and $h/L << 1$ where L is a characteristic in-plane length scale, e.g. the gap width R_o - R_i, (Howell 1996). The model also requires that the out-of-plane component of velocity is much larger than the in-plane component of velocity. Finally, under the stated assumptions, film stretching can be shown to be negligible at leading order such that h is constant and the film deforms in a sinuous manner. As a consequence and further to the information presented in table 1.1, clamped boundary conditions apply along the inner and outer boundaries so that H = 0 and $\frac{\partial H}{\partial r}$ = 0 when r = R_i or R_o. Following Howell's (1996) approach, the fluidic version of the (linearized) Foppl von Karman equation has the following form in cylindrical coordinates:

$$2\mu h\left(\frac{H_{r\theta}}{r}-\frac{H_\theta}{r^2}\right)\left(v_r-\frac{v}{r}\right)-\rho^- gH+(\Upsilon^+ +\Upsilon^-)\nabla^2{}_{\mathrm{H}}H=\frac{1}{3}\mu h^3\nabla^4{}_H H_t \qquad (1.6)$$

where, r and θ are cylindrical coordinates, ∇_H is the horizontal gradient operator $<\frac{\partial}{\partial \mathrm{r}}, \frac{1}{r}\frac{\partial}{\partial \theta}>$, t is time, g is the gravitational acceleration, γ^+ / γ^- is the surface tension along the upper / lower boundary of the film. Recall also that v is the azimuthal velocity. Here it consists of two components, namely a solid body rotation plus an irrotational vortex flow i.e.

$$v = \Lambda_1 r + \frac{\Lambda_2}{r} \qquad (1.7)$$

where Λ_1 and Λ_2 are real numbers having units s^{-1} and m^2/s respectively; Λ_1 and Λ_2 are determined by applying the no-slip boundary conditions along the inner (r = R_i) and outer (r = R_o) boundaries. If v varies linearly with r, terms of the form v_r - v/r as in term 1 of (1.6) vanish. Thus solid body rotation does not modify the wrinkle pattern described by the solution of (1.6). Therefore the former constant term, Λ_1, can be set to zero without loss of generality, which leaves

$$v = \frac{\Omega {R_i}^2 {R_o}^2}{({R_o}^2-{R_i}^2)r} \qquad (1.8)$$

Substituting (1.8) into (1.6) yields after some further algebra

$$\frac{4\mu h}{r^3}\,\frac{\Omega R_i^2 R_o^2}{R_o^2-R_i^2}\left(\frac{H_\theta}{r}-H_{r\theta}\right)-\rho^- gh+(\Upsilon^+ +\Upsilon^-)\,\nabla^2{}_H H=\frac{1}{3}\mu h^3\nabla^4{}_H H_t \qquad (1.9)$$

The first term on the left hand side of (1.9) describes the out-of-plane motion from in-plane stresses (compressive stresses drive buckling, tensile stresses oppose it). The second term is that of gravity and third term represents the surface tension; as explained by Ribe (2012), the impact of gravity and surface tension are most significant for long waves (small horizontal wave number). Ribe (2012) rationalizes this counterintuitive result regarding surface tension by noting that the forces associated with surface tension and the compression stresses are both inversely proportional to the square of the wavelength. Thus, "if [compression] exceeds surface tension for some wavelength (as it must if buckling is to occur) then it will do so for all wavelengths". Conversely, the term on the right hand side of (1.9) is due to the bending resistance whose effect is most pronounced for relatively short waves (large horizontal wave number). The bending resistance term is of a similar form in the analogous elastic membrane problem studied by Balmforth, Craster and Slim (2008), except that the Laplacian operator acts on *H* instead of its time derivative. In the problem at hand, H_t therefore vanishes when drawing the neutral stability curve of zero growth rate. In other words, whether we consider a rectilinear or an axisymmetric geometry, the bending resistance term can everywhere vanish in the case of a viscous film but not in the case of an elastic membrane. This has important mathematical implications which we discuss below.

In studying the free-surface wave pattern in the fluidic problem, the general methodology is to find the most unstable azimuthal wave number, m^*, to (1.9) as a function of R_i, R_o, h, Ω and μ, by proposing a normal mode solution. Thus m^* represents the azimuthal wave number having the largest associated growth rate. To this end, (1.9) is non-dimensionalized, scaling horizontal lengths with the outer radius R_o and vertical lengths with the (constant) film thickness h. Note that $\varepsilon = h/R_o$ where $\varepsilon \ll 1$ by the slender geometry approximation. Time t is scaled with the characteristic time scale T. Clearly the unit of T has to be the same as Ω^{-1}, so an obvious choice for T is $\sqrt{(h/g)}$; however this alternative has obvious difficulties for small angular speeds or very thin films. Thus we instead choose $T = \sqrt{(R_o/g)}$. The non-dimensional form of (1.9) then reads

$$\frac{12\Omega T}{r^3}\frac{\beta^2}{1-\beta^2}\left(\frac{H_\theta}{r} - H_{r\theta}\right) - \frac{3\Upsilon_1 H}{\varepsilon} + \frac{3\Upsilon_2}{\varepsilon}\nabla^2{}_H H = \varepsilon^2\nabla^4{}_H H_t \qquad (1.10)$$

where r and H are now non-dimensional variables. The geometric parameter β is the ratio of the radii, i.e. $\beta = R_i/R_o$. Moreover Υ_1 and Υ_2 are defined as follows

$$\Upsilon_1 = \frac{\rho^- g R_0 T}{\mu} \text{ and } \Upsilon_2 = \frac{(\Upsilon^+ + \Upsilon^-)T}{\mu R_o} \tag{1.11}$$

One may look for axisymmetric normal mode solutions to (1.10) of the form

$$H = f(r)\, e^{\sigma t + im\theta} + \text{c.c.} \tag{1.12}$$

where σ is the non-dimensional growth rate associated with azimuthal wave number m and c.c. denotes the complex conjugate. If $\sigma > 0$ (< 0), infinitesimal perturbations grow (decay) with time. The possibility of σ being a complex quantity was ruled out by Southwell and Skan (1924, page 592), who noted that equations of the type given by (1.10) are self-adjoint. Thus for the phase speed, C_p, of the waves, no theoretical prediction is possible because σ, as it appears in (1.12), is a real number. If σ was a complex number, then as shown in appendix D, the phase speed could be defined as σ_i/m where σ_i is the imaginary component of the growth rate.

Applying (1.12) in (1.10) yields the following differential eigenvalue problem

$$\frac{12\Omega T}{r^3} \cdot \frac{\beta^2}{1-\beta^2}\left(\frac{\mathrm{i}m}{r} f - \mathrm{i}m f\right) - \frac{3\Upsilon_1 f}{\varepsilon} + \frac{3\Upsilon_2}{\varepsilon}\left(f_{rr} + \frac{1}{r} f_r - \frac{m^2}{r^2} f\right) =$$
$$\varepsilon^2 \sigma \left(f_{rrrr} + \frac{2}{r} f_{rrr} - \frac{1}{r^2} f_{rr} - \frac{2m^2}{r^2} f_{rr} + \frac{1}{r^3} f_r + \frac{2m^2}{r^3} f_r - \frac{4m^2}{r^4} f + \frac{m^4}{r^4} f\right) \tag{1.13}$$

(c.f. equation 3.15 of Teichman 2002). One can solve equation (1.13) by adapting the spectral algorithms discussed in Weideman and Reddy (2000). By varying the independent non-dimensional parameters $\beta = R_i/R_o$, $\varepsilon = h/R_o$, ΩT, Υ_1 and Υ_2, σ as a function of m can be found. The value of m associated with the maximum value of σ is the most unstable azimuthal wave number and is denoted as m^*. Figure 1.6 shows the growth rates for different azimuthal wave numbers. The growth rate curve exhibits a global maximum for an intermediate value (not vanishingly small or infinitely large) of the azimuthal wave number.

Unfortunately, and as first pointed out by Benjamin and Mullin (1988), (1.10) is not devoid of degenerate behavior. Thus indefinitely large values of *m** are predicted when $\beta \rightarrow 1$, $\varepsilon \rightarrow 0$ or $\Omega T \rightarrow 0$. In the former case the gap width becomes vanishingly small so that the film cannot be assumed to be a small fraction of a characteristic horizontal length scale. Conversely when $\varepsilon \rightarrow 0$, the film itself becomes vanishingly thin. As a consequence, the bending resistance term of (1.10), whose damping effect is predominantly felt by short waves, disappears. In the absence of this term, perturbations of very short wavelength are able to grow which leads to the prediction of large values of *m**. Comparable observations apply to the latter case, $\Omega T \rightarrow 0$, wherein *m** again tends to infinity. It is important to note, however, that $\sigma \rightarrow 0$ as $\Omega T \rightarrow 0$ so that the infinitesimally small waves, whose physical relevance is clearly suspect, are at least predicted to grow indefinitely slowly.

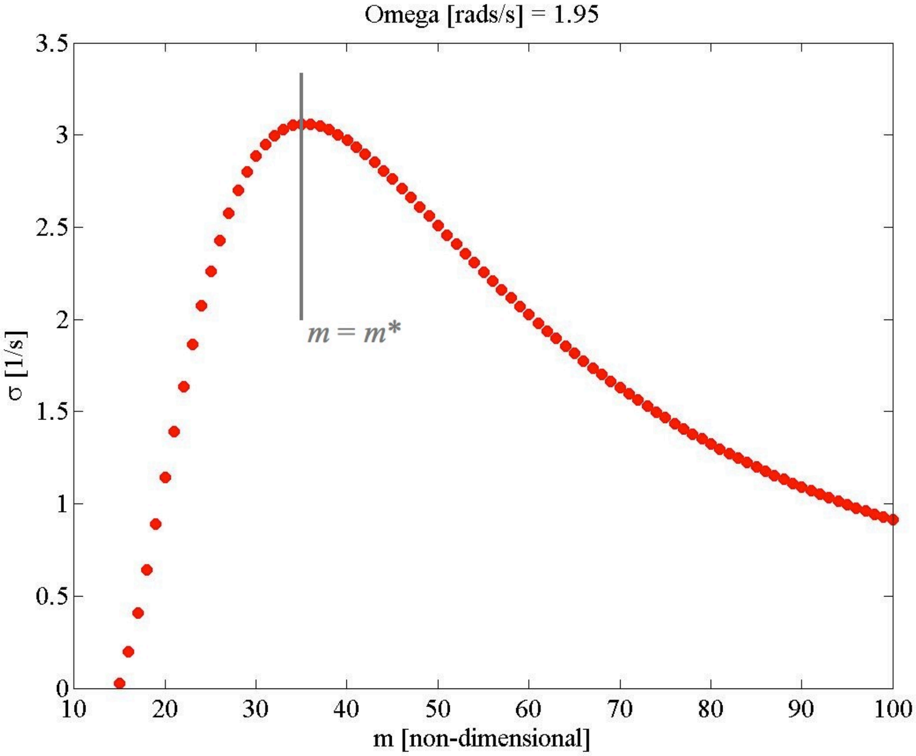

Figure 1.6: Growth rate vs. azimuthal wave number for a representative set of independent parameters. The solution is obtained by solving (1.13) using the spectral algorithms of Weideman and Reddy (2000).

Although (1.9) is unable to predict the conditions for the onset of buckling, it may be able to accurately predict m^* away from the point of onset. Assessing the accuracy of this claim is one of the principal goals of this thesis. To this end, the predictions from solving (1.9) are compared to results obtained from laboratory experiments, which will be discussed in great details below.

Note finally that because (1.9) is a linearized equation, perturbations to the uniform background state are assumed to be indefinitely small. As with phase speed, (1.9) is therefore unable to predict the wave amplitude. Any such prediction requires that a non-linear theory be developed. We shall return to this topic later in section 3.2.

1.3 Literature review

Having laid out the (asymptotic) theory describing the deformation of a viscous film in section 1.2, we can now proceed in summarizing those experimental, numerical and even observational investigations that form the background for the present research.

The motivation behind the earliest studies of viscous buckling was to gain an understanding of layered geological strata. These were modeled as highly viscous fluid layers with viscosities ranging from 10^{16} to 10^{21} Pa s. Biot (1961) investigated the two dimensional folding of viscous layers subjected to parallel compression. Relating viscous creeping flows to their elastic counterparts, he employed the Stokes-Rayleigh analogy to develop expressions for the critical load required for buckling and the wavelength of the associated instability.

The earliest experiments of note are those by Taylor (1969) where he studied shear induced viscous buckling in an annular geometry. A 10 mm deep film of golden syrup having a viscosity of 4000 cS floated on top of carbon tetrachloride, having a viscosity of approximately 1 cS, in a container of diameter of 150 mm. A horizontal disc of 55 mm diameter, immersed in the golden syrup, was rotated. At low angular speeds, the film of syrup remained flat. Taylor observed, however, that as the angular speed was increased beyond 0.37 r.p.s., small wavelength wrinkles could be seen on the free surface close to the disc, oriented at approximately 45^0 to its rim. The wrinkles disappeared a few seconds after the rotation was stopped, in accordance with low Reynolds numbers flows where inertial effects can be neglected. In the spirit of the Stokes-Rayleigh analogy, and consistent with the exposition of section 1.2, Taylor represented a theoretical interpretation based on elastic membrane approximations, which seemed to account for some of his aforementioned observations. However, and as we examine below, Taylor's theory and its later variants were subsequently criticized by other investigators.

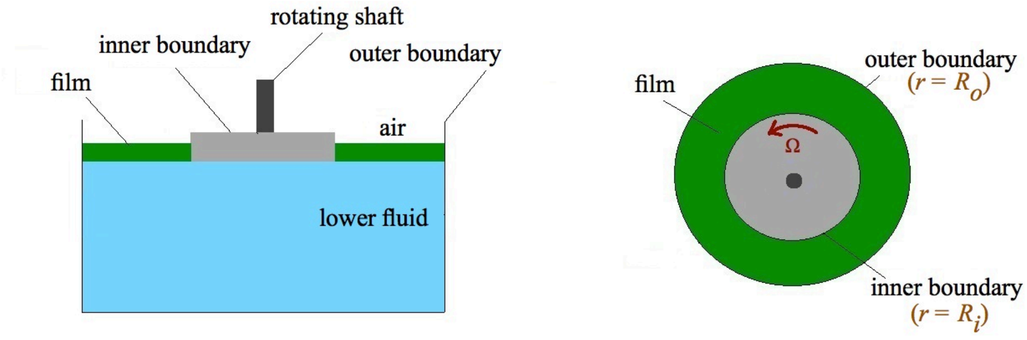

(a) (b)

Figure 1.7: The schematic of Taylor's experimental setup. (a) Partial side view and (b) top view.

Suleiman and Munson (1981) likewise presented experimental results for the buckling of a thin film of viscous liquid subjected to shear in an annular geometry. Consistent with the earlier study by Taylor (1969), they reported that when the dimensionless shear stress exceeded a critical value, the viscous film buckled similar to the buckling of a thin elastic plate.

In the experimental setup of Suleiman and Munson (1981) and in contrast to figure 1.7, a laterally constrained viscous film was subjected to annular shear by the rotation of the outer boundary while the inner one remained stationary. The torque required to rotate the outer cylinder was measured with a torsion wire from which the stationary inner cylinder was suspended. It was observed experimentally that the torque on the disc due to the bottom layer was negligible compared to that due to the much more viscous film. Silicone oil with kinematic viscosities of 10,000 - 100,000 cS and a specific gravity of 0.975 were used as the viscous film. Water, manometer fluid and mercury with specific gravities of 1.0, 1.75 and 13.6, respectively, were used as the bottom fluid.

Suleiman and Munson defined their shear stress as

$$\tau = \frac{M}{\pi R_i^2 h} \tag{1.14}$$

where M is the torque measured by the torsion wire, and $\pi R_i^2 h$ is the product of the area on which this shear stress acts and the moment arm.

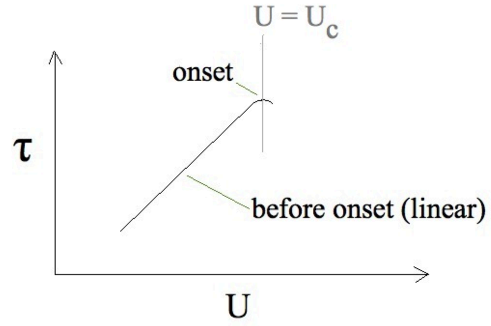

Figure 1.8: Determining the point of onset from the τ - U curve where $\tau = M / (\pi R_i^2 h)$ and $U = R_o \Omega$.

The point of buckling onset was determined in two ways: (i) by noting the point at which the free surface became distorted, and, (ii) by looking for a sudden change in the torque characteristics. As shown in figure 1.8, for low angular velocity, i.e. below the point of onset, the stress varied linearly with the angular velocity, Ω, and, by extension, the azimuthal velocity, $U = R_o\Omega$. However, at the critical angular speed, the τ - U relationship deviated from this straight line behavior.

If the film is unbuckled, and consistent with the notion that the air and water layers do not exert a traction on the oil, except through surface tension, the azimuthal velocity profile in the film should be similar to that prescribed by the classical axisymmetric Poiseuille flow problem. Therefore v is given by

$$v(r) = \frac{R_o^2\,\Omega}{R_o^2 - R_i^2}\left(r - \frac{R_i^2}{r}\right) \tag{1.15}$$

Note that Suleiman and Munson (1981) arrived at (1.15) by applying boundary conditions in much the same way as is discussed above vis-a-vis (1.8). In the narrow gap limit, the flow approaches a linear shear flow with shear stress

$$\tau = \mu U/b. \tag{1.16}$$

The experiments carried out by Suleiman and Munson (1981) were broadly of two types according to whether the narrow gap (relative to R_o) approximation was or was not valid. For a certain set of experiments from the former category, with $R_o = 12.6$ cm and the gap width $R_o - R_i = 1.27$ and 2.54 cm, the theoretical and experimental values of τ vs U were plotted. Theoretical values were based on a linear shear flow (narrow gap approximation) as discussed above in (1.16). Experimental values of shear stress were determined from (1.14). Suleiman and Munson's plots in this narrow gap regime indicate that the critical value of shear stress was nearly constant for all parameters; this included variation of the lower layer fluid and consequently, the net surface tension and specific gravity ratios. When the narrow gap approximation did not apply, i.e. $R_o = 5$ cm and $R_o - R_i = 1.27$ cm, it was observed that the critical shear stress value was independent of h only for $h/(R_o - R_i) < 0.2$, h being the film thickness. Suleiman and Munson (1981) also observed that the critical shear stress is, in general, unaffected by the depth, D, of the bottom layer. An important exception is the limiting case of a thin lower layer, i.e. as $D/(R_o - R_i) \rightarrow 0$, buckling became more difficult. When the lower layer was removed altogether, buckling did not occur.

Furthermore, Suleiman and Munson (1981) noted that the waves formed on the film surface travel in the direction of fluid motion with a phase speed of $C_p \sim 0.5\ \Omega$, where Ω is the angular speed of the rotating outer boundary. Increasing the angular speed much beyond its critical value $\Omega_c = U_c/R_o$ (where U_c is defined in figure 1.8) was accompanied by wave breaking. Sufficiently large values of angular velocity often led to the film being sheared apart.

Through a series of specific experiments having a Reynolds number of about 0.09, Suleiman and Munson (1981) noted how the variation of parameters such as the film thickness, gap width, film viscosity and angular speed affected the stability of the film. Thus an empirical correlation for the critical shear stress was developed in terms of the aforementioned parameters and the results were reported in the form of a dimensionless shear stress

$$\tau_c = \frac{\mu U}{(R_o - R_i)\surd(SG\,\gamma)} \qquad (1.17)$$

where SG is the specific gravity and γ is the net surface tension, which according to Davies and Rideal (1961) is simply the surface tension associated with a water - air interface in the absence of a film. Davies and Rideal (1961) obtain this result by the following reasoning: for two immiscible liquids, the interfacial surface tension, γ_b, is the difference between the surface tension of the two liquids with air, i.e. $\gamma_b = \gamma_2 - \gamma_1$, where γ_1 is the surface tension of the air-film interface and γ_2 is the surface tension of air-water interface. The net surface tension is then given by

$$\gamma = \gamma_1 + \gamma_b = \gamma_1 + (\gamma_2 - \gamma_1) = \gamma_2 \qquad (1.18)$$

Suleiman and Munson (1981) referred to the theory based on membrane approximations cited by Taylor (1969) according to which the film will buckle if the total normal stress in the film attains a negative value. Thus the onset of buckling is characterized by the following inequality

$$\gamma < h\tau \tag{1.19}$$

which, upon substituting $\tau = \mu U/b$ becomes

$$\gamma < \frac{\mu U h}{b} \tag{1.20}$$

Suleiman and Munson (1981) noted that this simple theory was unable to explain the buckling conditions from their experimental results. Rather, the empirical correlation described with reference to (1.17) was found to be more a consistent metric.

Seeking to add analytical and experimental clarity to the inconsistencies raised in the previous paragraph, Benjamin and Mullin (1988) conducted an independent investigation pertaining to the onset of buckling in a horizontal viscous film subjected to shear in an annular geometry. The critical value of dimensionless shear stress found experimentally was different than that observed by Suleiman and Munson (1981). Benjamin and Mullin (1988) also found a better agreement between experiment and theory, albeit using model equations based upon (1.1) and (1.2) rather than (1.6) or some variant thereon. Their aversion to equations of the Foppl Von Karman type is articulated when they write "As far as we are aware, an explicit account of the simple theory has not been given before, and its apparent success in explaining Taylor's observations has yet to be explained properly". Consistent with our previous remarks, Taylor's theory originates from equations of thin elastic plates that have been perturbed from their planar state (Timonshenko 1940, page 58). The bending stiffness of a thin elastic plate is given by

$$B = \frac{Eh^3}{12(1-v^2)} \tag{1.21}$$

where h is the plate thickness, E is Young's modulus and v is Poisson's ratio. For an incompressible material, $v = 1/2$ and $E = 3G$ where G is the modulus of rigidity. Thus the bending stiffness assumes the form

$$B = \frac{\mathrm{G}\, h^3}{3} \qquad (1.22)$$

According to Taylor's analysis, which motivates the discussion of section 1.2, the equilibrium equation of an elastic plate undergoing infinitesimally small perturbations is adapted to describe the deformation of an incompressible viscous film with dynamic viscosity μ. In concert with (1.22), the viscous resistance to bending is proportional to $(1/3)\mu h^3$ (c.f. the right hand side term in equation 1.6). The film is subjected to shearing at a rate, S, and the shear stress acting on the film is μSh, h being the film thickness. According to Benjamin and Mullin's interpretation of Taylor's theory, the general instability criteria is then given by

$$\mu|S|h > \gamma \qquad (1.23)$$

The wavelength of the most unstable mode is proportional to the square root of the difference between the right hand side and left hand side terms of (1.23). Consequently, the "waveform having maximum growth" has "indefinitely small" wavelength at the onset of instability.

Benjamin and Mullin (1988), having identified the deficiencies in Taylor's theory, developed their own model to predict the conditions for the onset of buckling. As noted above, Benjamin and Mullin's model is based on solving the full Stokes equations subject to the aforementioned kinematic and dynamic boundary conditions. However, no reference to boundary conditions at the inner or outer boundaries, such as no-slip condition, are found in their theoretical model. Rather a uniform shear rate, S, is assumed. The results are presented in the form of a dimensionless shear stress, τ, and a dimensionless film thickness, d, which are defined as follows

$$\tau = \frac{\mu S}{\surd\,(g\rho^{-}\gamma)} \qquad (1.24)$$

$$d = h\,\sqrt{\frac{g\rho^{-}}{\gamma}} \qquad (1.25)$$

The model predicts that buckling would occur when the dimensionless shear stress exceeds a certain critical value, τ_c, which depends on *d*. Benjamin and Mullin (1988) emphasize that when the instability condition is only marginally satisfied, the film may not be “prominently distorted by buckling”. Instead, the wrinkles would become “stronger” as τ is increased beyond τ_c. The model also predicts the condition for a secondary instability for long waves, for which the growth rates are too small for the waves to be seen in practical circumstances.

The experimental layout of Benjamin and Mullin (1988), although similar in concept, had some important differences when compared to that of Suleiman and Munson (1981). For instance, the inner boundary, which was a 20 mm thick circular aluminum disc with a radius of 140 ± 0.1 mm was rotated while the outer cylindrical boundary having a radius of 185 ± 0.1 mm was held fixed. As with the experiments to be discussed in chapter 2, the associated gap width of 45 ± 0.2 mm was large enough to render any meniscus effects insignificant because the wrinkles occurred away from the inner and outer boundaries. Also, the gap width being large compared to the radius, the rectilinear shear flow approximation was inapplicable, which contradicts the assumptions in their theory, which is based on a uniform shear rate and therefore a rectilinear geometry. Silicone oils with a specific gravity of 0.975 and kinematic viscosities of 10,000, 30,770 and 64,000 cS were used as the film fluid. A Sangymo Weston rheogoniometer was employed to measure the viscosity. Using this instrument, Benjamin and Mullin (1988) observed non-Newtonian effects in the 64,000 cS oil; these were manifest via the Weissenberg effect, which is illustrated schematically in figure 1.9.

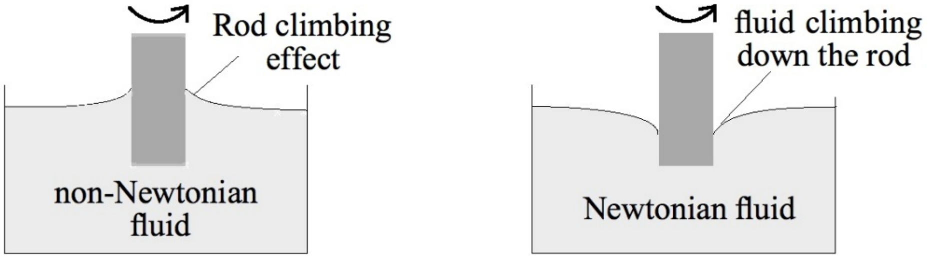

(a) (b)

Figure 1.9: The effect of spinning a rod in a non-Newtonian fluid vs. a Newtonian fluid. (a) A non-Newtonian fluid may exhibit a “rod climbing” effect also known as the Weissenberg effect whereas in a Newtonian fluid, (b) inertial forces predominate and the fluid moves down at the rod.

Experiments were conducted over several days starting with a maximum film thickness. Upon measurement of the critical speed for each film thickness, small quantities of oil were removed making the film successively thinner for each experimental run. This process was repeated until the film attained a thickness where it ruptured easily upon attempts to remove any further oil. Care was taken so that the film surface was smooth before each trial run. The thickness of the film was measured using a micrometer controlled depth gauge with an accuracy of up to ± 0.04 mm. Assuming that the annular film was uniform and that hydrodynamic effects in the water below are negligible, the expression relating the azimuthal velocity, v, and r reads

$$v(r) = \frac{R_i^2\,\Omega}{R_o^2 - R_i^2}\left(\frac{R_o^2}{r} - r\right) \tag{1.26}$$

Thus the shear stress in the film is given by -μS where

$$S = -\frac{\mathrm{d}v}{r} + \frac{v}{r} = \frac{2\,\Omega\,R_i^2\,R_o^2}{(R_o^2 - R_i^2)\,r^2} \tag{1.27}$$

Qualitatively speaking, Benjamin and Mullin (1988) observed similar buckling patterns as did Suleiman and Munson (1981). The film remained “featureless” until a critical angular speed, Ω_C, was reached. This critical speed depended on the film thickness, h, and the viscosity, μ. At the critical speed, wrinkles were seen on the film surface oriented at approximately 45^0 to the edge of the disc. With a further increase in the angular speed, the wrinkles became more prominent; in the words of Benjamin and Mullin (1988), "both their amplitude and radial extent increased steadily". They argued that their method for determining the point of onset was better than that of Suleiman and Munson (1981). In Benjamin and Mullin's experiments, illumination from below by a diffused light source cast an image of the film surface on the ceiling. The appearance of a regular pattern of shadows in the image on the ceiling was considered to represent the onset of buckling. Benjamin and Mullin (1988) reported that the values of Ω_C so obtained were reproducible to within 1% error in successive trials; no hysteresis effects were observed. The critical value of shear stress reported by Benjamin and Mullin (1988) is almost half of that found by Suleiman and Munson (1981). The former group argued that their results are more accurate because their method of determining the point of onset of buckling is more sensitive than that of the latter group. More specifically, Benjamin and Mullin (1988) argue that Suleiman and Munson (1981) could have erroneously judged a "subsequent stage in the development of buckling" as the point of onset. Benjamin and Mullin (1988) also highlighted that their experimental results, when compared to those of Suleiman and Munson's (1981), benefited from a larger gap width, which minimized meniscus effects, and also a wider range of film thickness values.

In comparing experiment and theory, Benjamin and Mullin (1988) plotted results of the dimensionless shear stress defined by (1.24) against the dimensionless thickness defined by (1.25). For the lower viscosity oils, i.e. 10,100 and 30,770 cS, good agreement was noted. However for the film viscosity of 64,000 cS, the experimental points were 60% higher than their theoretical counterparts for $0.4 < d < 0.9$. Benjamin and Mullin (1988) attribute this lack of agreement to the aforementioned Weissenberg effect; they write "the observed thickening of the sheared layer at its inner edge, which implies thinning of the layer elsewhere, is a complication presumably insufficient to invalidate the present theoretical model." Their attempts to account for non-Newtonian effects theoretically were "inconclusive".

The next significant investigation in this field was made by Teichman (2002), who, in a portion of his doctoral research "motivated by analogous scenarios in elasticity", likewise studied the wrinkling behavior of an annular viscous film subjected to shearing. A theoretical model was developed, results from which were compared against experimental measurements, with the emphasis again being on the point of onset of buckling. Notwithstanding Benjamin and Mullin's (1988) critiques, the model in question represented a return to (asymptotic) models of the type popularized by Taylor, i.e. it had many similar features to that of section 1.2 as we outline below. Interestingly, Teichman (2002) appears not to have fully understood Benjamin and Mullin's critiques because he erroneously claims that his asymptotic model is able to predict the critical angular speed associated with the onset of buckling. This supposition is false for the reasons outlined in section 1.2. Elsewhere, Teichman (2002) found the most unstable azimuthal wave number, m^*, from a normal mode analysis of (1.9). He remarked that, "in the real world, perturbations are always present, so the small amplitude analysis here will elucidate the early behavior and stability of the sheet as it diverges from its initially planar form."

Although the dimensional governing equation examined by Teichman (2002) was identical to (1.9), he followed the approach of Buckmaster, Nachman and Ting (1975) in scaling this result. Teichman's non-dimensional equation is therefore different from (1.10). More specifically, in Teichman's case, horizontal and vertical lengths were scaled with L and εL respectively, where $\varepsilon << 1$ and L is an in-plane length scale whose precise value is not specified. (In section 1.2 by contrast, the definition of L is unambiguous: $L = R_o$)

Experimentally, Teichman (2002) employed a similar layout and procedure to the ones discussed above. A laterally constrained annular viscous film was subjected to shear by the rotation of an inner cylinder as the outer cylinder remained fixed with a radius of R_o = 14.1 cm. In this respect, Teichman (2002) used different geometrical configurations by varying the radius of the inner boundary. Pre-heated viscous fluid, Amoco Indopol H-300, was used to form a film of thickness 2 mm. Teichman chose this value of film thickness because the capillary length of the oil was slightly less than 2 mm; thus for films with h < 2 mm, film rupture was anticipated even at relatively low shear rates. A video camera was used to record the experimental images. The number of waves or wrinkles seen on the free surface at the onset of buckling was counted from the recorded video images and the corresponding angular speed was obtained from the motor controller.

In his figures, Teichman (2002) compares experimental results of the azimuthal wave number, m^*, with those predicted by his theoretical model, at a particular value of angular speed which he considers to be the critical value. The experimental results agree with the theoretical predictions of m^* for $R_i/R_o < 0.2$. For $R_i/R_o > 0.2$, however, there is poor agreement between experiment and theory with the theoretical predictions being almost twice the magnitude of the experimental points. Teichman (2002) provides several possible explanations for this discrepancy. Firstly, his theory is an asymptotic one derived in the limit of very small film thickness; results may deviate from theory for films having finite h. Secondly, although the angular velocity was increased slowly, the response of the film could still have been transient, an effect ignored by the model equations. Finally, at the exact point of onset, the wrinkles were infinitesimally small. In the practical world, such small wrinkles would be impossible to see by the naked eye and hence the experimentally detected “onset” could have coincided with a region beyond the actual point of buckling, i.e. where the waves are large enough to be visible. This argument is of course similar to the one presented by Benjamin and Mullin (1988) when they criticize the findings of Suleiman and Munson (1981).

Teichman's thesis also examined film buckling in a rectilinear, rather than an axisymmetric, geometry. This analysis contained a number of nontrivial errors, however, so we refer instead to the follow-up investigation of Slim et al. (2012) in which these errors were corrected and further results described. To this end, two models were considered; the first one, similar to the theoretical model described by (1.9), was an asymptotic theory for the dynamics of a viscous film. The second, more complete, model came from numerically solving the full Stokes equations i.e. (1.1) and (1.2).

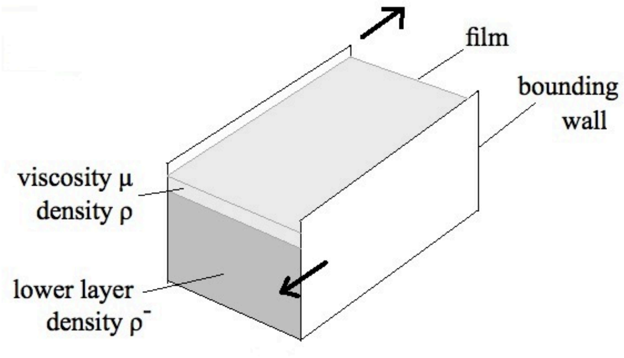

Figure 1.10: Viscous film sheared by the moving bounding walls.

As shown schematically in figure 1.10, a Newtonian fluid of finite width and infinite length was considered as the viscous film, which floated atop a deep lower fluid. Contrary to the case when the film occupies the entire channel depth, which is linearly stable under all values of the shear rate, this thin film buckled when the sidewalls were moved at different speeds. Expanding on the work done by Teichman in 2002, Slim et al. (2012) present the conditions for the onset of buckling for this plane Couette geometry by examining solutions to (1.1) and (1.2). Beyond onset, estimates of the wavelength and growth rate of the most unstable mode are given. The output of the model based on the full Stokes equations for the mode profile and wavelength of the most unstable mode at onset matches that of the asymptotic theory for films having an aspect ratio up to 0.04.

However, for aspect ratios in excess of this value, the respective predictions diverge. The model based on the full Stokes equations shows that a film with an aspect ratio of 0.6 is the thickest film that can be buckled. This model also establishes the relation between the critical wall speed and other parameters such as the thickness of the film and the surface tension coefficients. In a concluding note, Slim et al. (2012) remark that although some experiments by Suleiman and Munson (1981) approach the rectilinear flow limit, an annular flow configuration is fundamentally different from a rectangular Couette flow due to the presence of an additional length scale, i.e. that associated with curvature. Slim et al. (2012) therefore suggested that some of the aforementioned degeneracies associated with asymptotic models may apply in a rectilinear geometry, but not an axisymmetric one. In the latter case there are two canonical lengths, namely the gap width and the inner or outer radius. In fact, in Bhattacharya, Craster and Flynn (2012), whose theoretical considerations have been highlighted in section 1.2, it is argued that the axisymmetric problem shares the same degeneracies as the rectilinear problem.

1.4 Contribution of the present research

Building on Taylor's (1969) classical experiments and also the subsequent work of other researchers which we reviewed above, here we perform a similar series of experiments to study the shear induced buckling of a thin, viscous film in an axisymmetric geometry. Shear is generated in a horizontal film of silicone oil, floating atop a deeper layer of water, laterally constrained in an annular geometry, due to the rotation of the inner boundary relative to a fixed outer one. Consistent with Taylor's experiments, upon exceeding a critical value, the shear forces excite out-of-plane displacements in the film, manifest as wrinkles on the free surface. The experimental data is captured by a camera and the associated images are post-processed in MATLAB.

Our aim is therefore to characterize the variation of the following dependent parameters: the number, m^*, relative speed, C_p/Ω, and amplitude, A, of the waves excited at the free surface. Experimentally, m^* is the number of waves that can be seen at the free long the perimeter of the disc assembly. The independent parameters are: (i) the film kinematic viscosity, ν, (ii) h, (iii) R_i/R_o and (iv) Ω. Detailed figures and descriptions are provided in chapter 2.

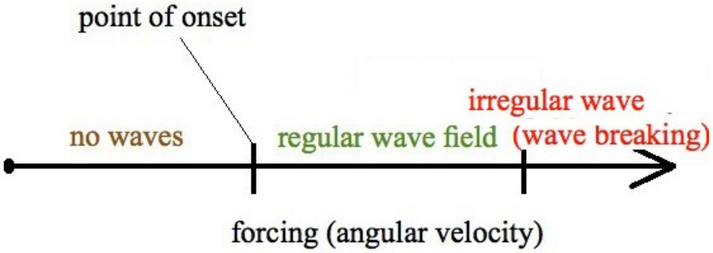

Figure 1.11: The different regimes of film behavior depending on the applied forcing.

At this stage, it must be mentioned that the present research, although similar in spirit to the previous investigations of Suleiman and Munson (1981), Benjamin and Mullin (1988) and Teichman (2002), has some prominent differences. The focus of these prior investigations was largely on the point of buckling onset. Thus Suleiman and Munson (1981), Benjamin and Mullin (1988) and Teichman (2002) all experimentally measured the critical shear associated with onset. It is unclear, however, the extent to which an asymptotic model (i.e. of the type based on the Foppl von Karman equation) yields accurate predictions away from this point of onset. We wish to study this question by rigorously comparing model predictions of m^* with experimental data for the axisymmetric case. Thus, referring to figure 1.11, the primary focus of the present research is not on the point of onset, but rather on the regime beyond onset but before wave breaking. As part of this investigation and consistent with the above remarks, m^* and C_p/Ω are to be experimentally determined. Also, for the first time, experimental results for the wave amplitude will be reported. Note that only experimental results have been presented for the relative speed, C_p/Ω, and the wave amplitude, A; no theoretical predictions are possible in this case, at least not using the linear, self-adjoint theory based on the Foppl von Karman equation.

Although a brief summary of these equations has been presented earlier in section 1.2, my principal contribution (and therefore the focus of this thesis) concerns the design, execution, post-processing and interpretation of the experiments rather than the detailed analysis of the model equations. Thus curves showing theoretical predictions of m^* are included in chapter 3 principally for the point of making comparisons with the experimental data.

1.5 Thesis organization

The rest of the thesis is organized as follows: chapter 2 provides a detailed summary of the equipment used in the laboratory, the operating procedure for the experiments, how each experiment is setup and run, and how measurements are made. It also explains the optical system used to capture the experimental images and the post processing techniques employed to obtain results using MATLAB. In chapter 3, results are presented and analyzed. The thesis ends with chapter 4, which summarizes all the work that has been done, the challenges faced and by examining possible future work that can take this research to the next step.

Note finally that components of this thesis, in particular the experimental data of Chapter 3, have been incorporated into a manuscript submitted in May 2012 to *Physics of Fluids* I am listed as the lead author of this manuscript (the second and third authors are, respectively, Dr. Richard Craster of the Imperial College London and Dr. Morris Flynn).

Chapter 2 - Experiment and post processing

This chapter is divided into two parts. The former part considers the measurement of the number of waves, m^*, and the relative speed, C_p/Ω, whereas the latter part examines measurements of the wave amplitude, A.

2.1 Wave count and relative speed

2.1.1 Equipment

Figure 2.1 shows the glass beaker used in the present experiments. The beaker has a circular cross section (dimensions given in table 2.1). Figure 2.1 (a) shows the side view across a vertical plane passing through the center of the beaker. Figure 2.1 (b) shows the top view. The rotating inner boundary is referred to as the disc assembly and is composed of four principal elements (i) a metal disc, (ii) a metal ring attached to the perimeter of the disc, (iii) a disc assembly shaft and (iv) a collar. The beaker contained an inner concentric glass annulus with a cylindrical base plate, which itself had a circular brass groove cut into it. As shown in figure 2.1 (c), the protruding shaft of the disc assembly sat inside this groove. Lubrication was provided to ensure smooth rotation.

The glass beaker was filled with water (shown in blue) to a level such that it was just above the outside corner of the perimetric ring. The depth of the water layer, denoted by D, was 14.0 ± 0.1 cm.

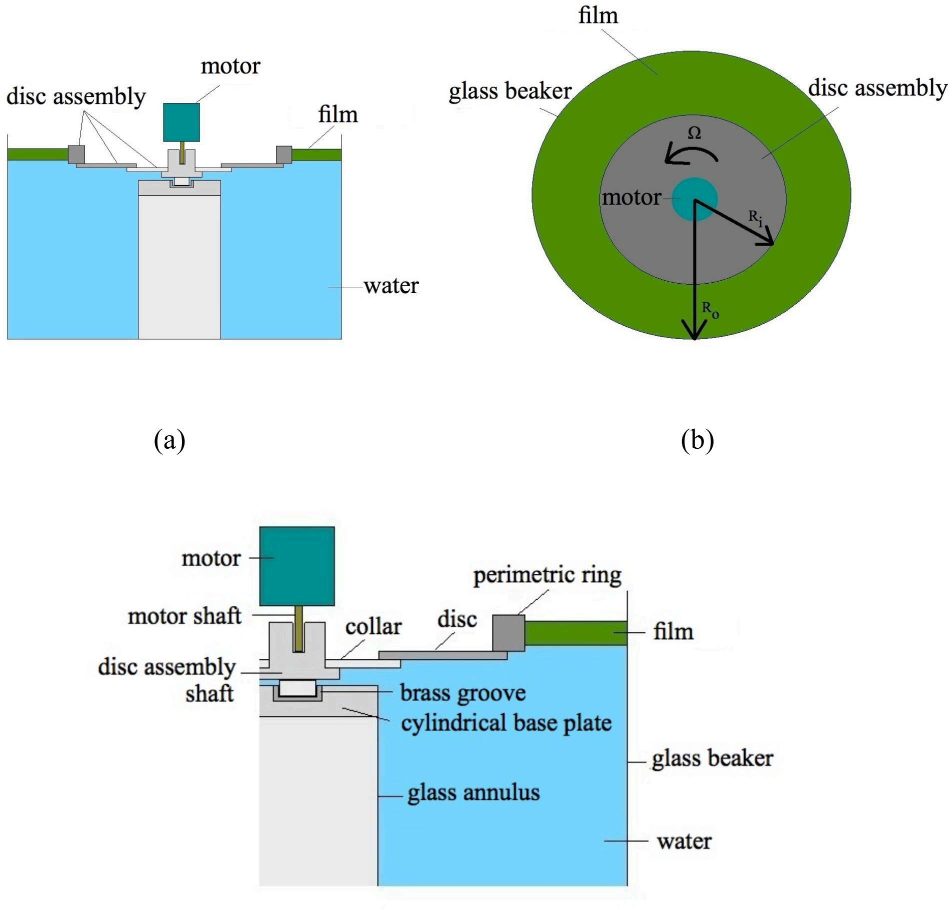

(a)

(b)

(c)

Figure 2.1: Glass beaker (a) side view, (b) top view and (c) magnified side view.

The perimetric rings had a height of 12.7 mm. Because the maximum film thickness was less than 5 mm, the film was in contact only with the vertical outside edge of the perimetric ring and did not flow above or below the ring. Three disc assemblies were used in the experiments and their dimensions are summarized in table 2.1. The beaker diameter being fixed, the different disc assemblies allow for different geometric configurations, i.e. different values for $\beta = R_i/R_o$. The advantage of using perimetric rings rather than discs with a uniform thickness of 6.35 mm lay in weight saving and hence a lighter load on the motor.

Table 2.1: Dimensions of the glass beaker and metal disc assemblies. Note that R_i and R_o are defined in figure 2.1 (b), i.e. R_i is the outer radius of the perimetric ring and R_o is the inner radius of the glass beaker.

Equipment	**Radius (± 0.5 mm)**	**$\beta = R_i / R_o$**	**Error in β**
Glass beaker	147.0		
Disc A	73.0	0.497	0.005
Disc B	98.0	0.670	0.005
Disc C	124.0	0.840	0.006

The glass beaker was supported on the adjustable frame as shown in figure 2.2. The frame consists of interlocking pieces of 80-20 T-slotted aluminum bars, which offer the necessary structural rigidity and are, moreover, resistant to corrosion.

Table 2.2: Properties of the film in comparison to water.

Property	**Film (silicone oil)**	**Water**
Thickness	1.95 - 4.95 mm	140 mm
Viscosity	12,500 and 30,000 cS	1 cS
Specific gravity	0.97	1.0

Table 2.3: Film viscosities.

PMX 200 Silicone oil (Specific gravity 0.97)	**Viscosity (cS)**
PMX 200 - 12500	12,500
PMX 200 - 30000	30,000

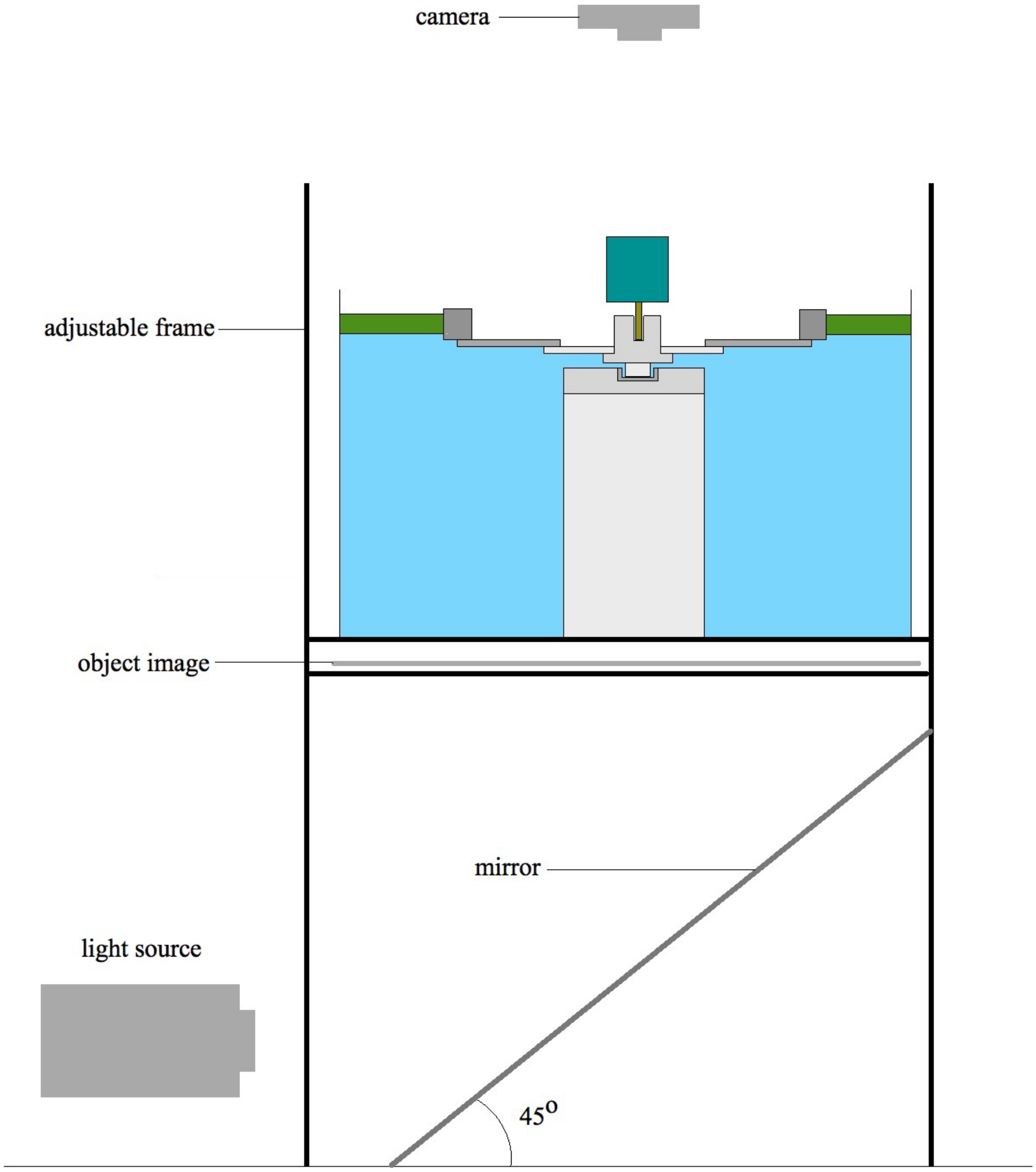

Figure 2.2: The experimental setup. Note that the position of the camera and the light source relative to the beaker is not to scale.

Two types of silicone oil, listed in table 2.3, were used as the film fluid. These were manufactured by Xiameter, who in turn provided information on the relevant material properties (density, viscosity, etc). This particular fluid was chosen because it was non-toxic and was available in a wide range of viscosities. Silicone oil had been used in earlier experimental investigations, e.g. by Suleiman and Munson (1981) and Benjamin and Mullin (1988). Prior to using the silicone oil, experiments were carried out using a series of polybutene oils with an approximate viscosity range of 1000 to 20,000 cS. However, the Indopol oils were discarded as it was difficult to excite a wave field that remained regular for a sufficient period of time in which readings could be taken.

The film (specific gravity 0.97) floated on top of the water surface (specific gravity 1.0) and had a thickness between 1.95 and 4.95 mm. Film thickness of more than 4.95 mm was avoided because a regular wave field was not easily excited in the associated experiments. Conversely, it was observed that a film thickness less than 1.95 mm caused the oil layer to rupture or easily separate, thereby exposing the water below. Referring to Teichman's (2002) discussion, holes are expected to form in the film if the thickness is significantly less than the capillary length, $\lambda = \sqrt{(\gamma/\rho g)}$, where γ is the net surface tension. For the present research, the capillary length was found to be 2.15 mm, which is close to the minimum film thickness of 1.95 mm for the present experiments.

Variable speed DC motors, manufactured by Servocity, were used to rotate the disc assemblies. The motor speed was adjusted by varying the applied voltage using a potentiometer manufactured by the technical services group in the Department of Mechanical Engineering. At a particular applied voltage, the motor speed was constant. This was verified from a sequence of images of the rotating disc assembly taken by a high speed camera, specifications for which are given below. In particular, the number of frames between consecutive full rotations of the disc was constant to within 2% or less.

Table 2.4 lists the three motors employed to rotate the disc assemblies and also specifies the weight of each assembly, which provides an indication of how much load was applied to the corresponding motor. The larger the torque of the motor, the heavier (larger) the disc assembly for which it was used. Consistent with the aforementioned studies of Suleiman and Munson (1981), Benjamin and Mullin (1988) and Teichman (2002), the perturbations in the fluid layer appeared only after a certain threshold angular speed had been surpassed. For disc assemblies with comparatively smaller radii, a higher r.p.m. motor was necessary to reach the required tangential speeds. As shown in table 2.4, the slower motors having higher torque were therefore reserved for the larger disc assemblies whereas the faster motors having lower torque were used for the smaller disc assemblies.

Table 2.4: DC motor and disc assembly specifications.

Maximum motor speed (rpm)	Torque (oz.in)	Application	
		Disc assembly	Assembly weight (kg)
20	375	C	1.35
45	278	B	1.00
90	139	A	0.70

A straightforward optical setup (figure 2.2) was used to capture images of the disc assembly and wave field in motion. It consisted of a high speed camera, a light source, a mirror and a pattern of horizontal and vertical lines printed on plain white paper. The following paragraphs describe the role of each component in detail.

The Redlake MotionPro is a high speed camera capable of up to 10,000 fps (frames per second) at 256 x 48 pixels and 500 fps at 1280 x 1024 pixels. It is a monochrome unit with a data depth of 8 bits, i.e. each pixel can store 2^8 different levels of intensity values; in other words, 0 for black and 255 for white. The images were viewed using Redlake Midas software. The software was also used to control various parameters of the camera such as frame size, frame rate, trigger properties, etc.

Mounted on a tripod, the camera looked vertically down at the center of the beaker. It was centered on the axis of the disc assembly by hanging a plumb bob from the center of the lens. More precisely, the camera was at a distance of 78.50 ± 0.05 cm above the oil surface. Using a Nikon 35 mm f/1.8 lens, the horizontal plane encompassing the film surface was brought into focus.

A frame size of 1024 x 768 pixels was chosen because, at the given distance from the fluid surface, it covered just over one half of the film surface. The other half of the film surface was obstructed from view by a clamp that was used to secure the motor in place. Results for $m*$ were obtained by counting the number of wave troughs or crests in the experimental images and then multiplying by two. To this end, the specific values of the object distance and frame size, as listed above, were chosen.

A Kodak slide projector was used as the light source. As shown in figure 2.2, a mirror oriented at approximately 45^0, was used to reflect the light vertically upwards. To complete the optical arrangement, the grid of horizontal and vertical lines, referred to as an object image or grid pattern, was placed just below the beaker. The grid pattern served two purposes. Firstly, the opacity of the paper dimmed out some of the glare from the projector bulb, which made the recorded images more uniform in intensity and therefore easier to interpret and process. Secondly, the grid pattern aided in visualizing the surface deflections to the viscous film in the image processing, details of which are given in section 2.1.3. The line spacing and thickness were carefully chosen to optimize the identification of wave crests and troughs. Each line is 1 mm thick and is at a distance of 4 mm from its nearest parallel line.

2.1.2 Experimental procedure

This paragraph describes the process of setting up the experiment in sequential order. The glass beaker was set on the frame as shown in figure 2.2. After filling it to a depth of 14.0 ± 0.1 cm with warm tap water, it was left undisturbed overnight. Small air bubbles, which appeared on the inner wall of the beaker, were scrapped off to avoid them from getting trapped in the oil layer which was added subsequently. The required disc assembly was fixed in place and connected to either the 20, 45 or 90 rpm motor as per the guidelines presented in table 2.4. Thereafter a measured quantity (by mass) of the silicone oil was poured on top of the water. The mass of oil was used in determining the film thickness, h, and corresponds to the difference between the mass of the oil in a small plastic beaker before pouring and the mass of the residual oil and the beaker after pouring. For this purpose an Acculab Vicon balance was used that is accurate to 0.01 g. The film thickness, h, was calculated by the following equation:

$$h = \frac{q}{\rho \pi (R_o^2 - R_i^2)} \qquad (2.1)$$

where q and ρ are, respectively, the mass and density of the oil. The oil spread as the disc assembly was slowly rotated to form a continuous film. The film was then allowed to rest for at least eight hours till a smooth surface, devoid of obvious patches of uneven height, could be seen. The object image was placed on the frame, just below the beaker and the camera was set vertically above the motor.

The relevant parameters such as the inner radius R_i, oil kinematic viscosity, ν, and film thickness, h, were noted for each experimental setup. Different trials were performed by varying the angular speed, Ω, of the disc assembly. For each trial, the frame rate or camera speed was also recorded because this quantity was required to calculate Ω. Typical values of Ω fell between 0.50 and 4.30 ± 0.12 rad/s.

By adjusting the voltage across the motor using the potentiometer, the motor speed was gradually increased to a point where a regular wave field, consisting of waves of regular size and spacing, was observed at the free surface. With the light source being ‘on’, the camera recorded the data and a sequence of images was thereby saved to the computer. Each data set was gathered over a sufficient time interval, typically 15 - 20 s, to ensure that the wave field was consistent and not a mere transient response to the imposed shear. Conversely, an interval of least 30 minutes was kept between trials to ensure that the film had returned to its smooth and quiescent initial state. Hysteresis effects, as described in the following sentences, were observed if a particular trial was run for a time period much longer than the aforementioned 15 – 20 s and also if a sufficient resting interval was not provided in between consecutive trials. An extended trial run, say a few minutes in duration, was characterized by prominent changes in the wave pattern. These included the merging of adjacent waves, the wave field disappearing altogether and the film being torn into two separate regions with one part rotating with the disc assembly and the other remaining afixed to the outer glass wall. If multiple trials were run back to back without allowing the system to return to a fully quiescent state, the wave field was observed to be excited at lower angular speeds than expected. After several trials with different Ω for a particular experimental setup, a different experiment was run with new values of ν, h and/or R_i/R_o. The glass beaker and disc assemblies were wiped clean and dry to ensure that no residual oil remained to contaminate subsequent experiment(s).

2.1.3 Post processing

By adopting various post processing methods, the goal was to determine the following for each data set: the wave count, m^*, and the angular speed of the waves with respect to the disc assembly, C_p/Ω.

Although the dial on the potentiometer provides a rough idea of the motor speed, there is no direct way of obtaining a highly precise value of Ω in a particular experiment. Thus Ω was instead determined as follows: each disc was marked at known angular intervals, for example with electrical tape. While progressively scanning through the image sequence, the frame numbers were noted down as each tape mark crossed any chosen fixed point in the image. The interval between such frame numbers (averaged over many readings) gave the number of frames, n, taken by the disc to complete one full rotation, which when combined with the frame speed, *f*, of the camera gave the angular speed as

$$\Omega = \frac{2\ \pi\ f}{n} \tag{2.2}$$

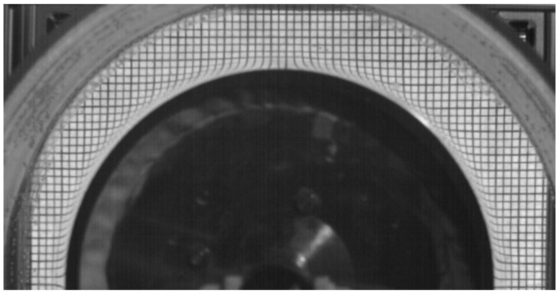

Figure 2.3: At $t = 0$, disc assembly B is at rest and no waves appear at the free surface.

The technique used to determine m^* is as follows. Experimental images were read into MATLAB and cropped as necessary. Figure 2.3 shows an image taken when the disc is stationary and hence, no waves can be seen at the free surface. Let us say this is at time instant $t = 0$. Note that a deflection of the free surface, due to meniscus effects, is evident near the perimeter of the disc assembly. Consistent with the experiments of Benjamin and Mullin (1988), however, this deflection is not believed to have a significant impact on our measured data because the free surface waves occur at a radial distance beyond the region of meniscus deflection. This is illustrated by figure 2.4 (a), which shows an image taken at $t = t_1$ when the disc is rotating; a regular wave field can be seen at the free surface with the troughs and crests oriented at approximately 45^0 to the outer edge of the disc assembly, which is consistent with the observations of previous research groups such as Taylor (1969) and Benjamin and Mullin (1988). Figure 2.4 (b) shows an image captured at $t = t_2$, a short time later; for the range of experiments discussed here, we chose $t_2 - t_1 = 0.02$ to 0.04 s. Correspondingly, from one frame to the next, the disc assembly rotated by a small angle, in an approximate range of 1 to 4^0. As a consequence, the wave field rotated by approximately 2 to 6 pixels (measured approximately at the point where the wave amplitude is believed to be the largest), depending on the phase speed of the waves and the disc assembly radius.

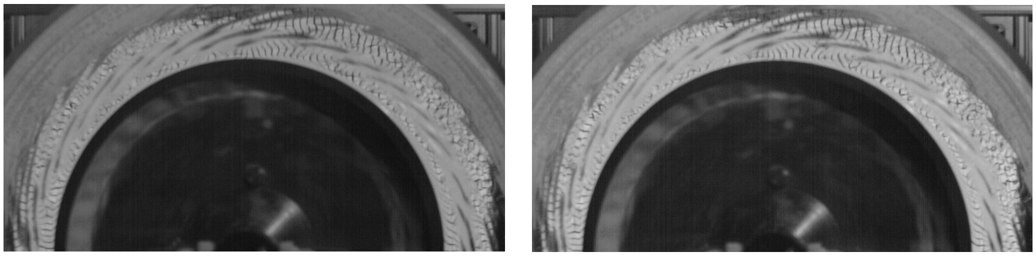

(a) $t = t_1$ (b) $t = t_2$

Figure 2.4: At $t = t_1$ or $t = t_2$ where $t_2 > t_1 > 0$, the disc assembly is in motion and a regular wave field is apparent.

Subtracting the former image from the later gave the angular displacement of the troughs and crests between time instants $t = t_1$ and $t = t_2$. The subtracted image was thresholded, whereby the intensity of those pixels corresponding to a displaced trough or crest were increased so as to amplify the signal. Conversely in instances where the pixel intensity fell below a prescribed threshold, the pixel intensity was set to zero. The final result is shown in figure 2.5. The conceptual equation for this process is given as follows:

$$\mathbf{Image}\ (t{=}t_2)\ \mathbf{-\ Image}\ (t{=}t_1) \xrightarrow{\textit{thresholding}} \mathbf{Final\ Image} \qquad (2.3)$$

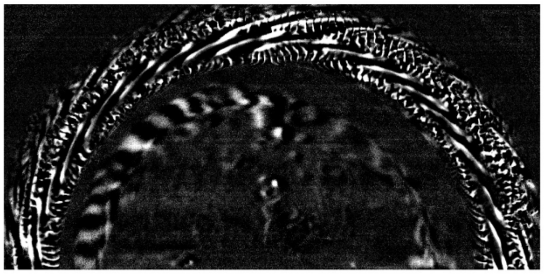

Figure 2.5: Result after subtracting the two images from figure 2.4.

In figure 2.5, the spiral white regions in the film, between the inner and outer radii, along the perimeter of the disc assembly show the rotation of the individual wave troughs. At this stage, each wave can be uniquely identified and the number of waves within each image counted. Because the images do not show the entire free surface of the film but rather one-half of this surface, the wave count obtained from images like figure 2.5 is, as noted above, multiplied by a factor of two. Multiple image pairs were taken where each image pair is 1 s apart from the next. The wave count was averaged over all these samples to give the final experimental wave count, m^*, for a particular trial.

Note that the wave count so obtained after image processing is much more accurate than what might be derived by rudimentary visual inspection of figures such as 2.4 (a) and 2.4 (b) because the unprocessed images do not always have the necessary clarity required to directly count wave troughs and crests. In other words, the post processing algorithm amplifies small changes in intensity, thus facilitating the determination of m^*. In a similar spirit to Schlieren techniques (eg. Moisy et al. 2005), the thickness and spacing of the grid lines in the object image placed below the glass beaker were carefully chosen so as to enhance the appearance of deflections to the free surface.

The algorithm described above can be qualitatively compared to Particle Image Velocimetry (PIV) or Particle Tracking Velocimetry (PTV) (Adrian, 1991). In principle, the image subtraction embodied by (2.3) is similar to the operations performed by PIV or PTV, wherein measurements are based on the displacement of a particle or group of particles between two successive images that are separated by a known time interval. Note, however that PIV or PTV are methods for estimating the fluid velocity, which is not our focus here.

Although the camera is capable of speeds up to 10,000 fps, an optimum value of 100 fps was chosen for the following reasons. With an increase in the frame rate, the amount of light entering the camera decreases, which leads to darker images.

It also adds more noise to the images. Both these factors complicate the image processing work that is done in MATLAB. Thus, with respect to the camera and lighting conditions in the laboratory, the lower the frame rate, the better exposed the images will be. However, in the experiments, the waves may have a considerable phase speed (up to 2 rad/s). If the frame rate is too low, then between one frame and the next, a particular wave may be rotated by an amount greater than $2\pi/m^*$. This would render the aforementioned wave counting process unreliable as the displacement of a wave might equal or even exceed its wavelength, which would enable a wave crest to align itself with an adjacent crest in the time interval between consecutive images.

Taking the factors listed above into consideration, an intermediate optimum value of 100 fps was selected which ensures that the images have adequate intensity, relatively low noise and also that the wave field does not rotate by more than a fraction of $2\pi/m^*$ from one image to the next.

The phase speed, C_p, of the waves is less than that of the disc, Ω. This is consistent with the previous experimental investigation by Suleiman and Munson (1981) where a value of $C_p \sim 0.5\ \Omega$ was reported. The ratio of angular speeds, is termed the 'relative speed' here. This ratio is the same as the ratio of the number of waves crossing a reference point in one full rotation of the disc, which is noted by observing a sequence of images, and the wave count, m^*, previously obtained by image subtraction. The method for determining the phase speed is thus similar to that for determining the angular speed.

2.2 Wave amplitude

As with C_p, we cannot get an estimate of the wave amplitude, A, from the theory outlined in section 1.2. For fixed β, we therefore rely on experimental measurements to estimate the dependence of A with Ω, h and ν. The aim is to measure the amplitude of the free surface deflections by a non-intrusive technique. To this end, several candidate methods were considered. First among these was a free-surface synthetic schlieren method presented by Moisy et al. (2005), which is an optical technique that can measure the instantaneous topography of the interface between two transparent fluids. In Moisy's experiments, the refracted image of a random dot pattern, placed below the flow tank (similar to the object image used in our experiments), was captured by a camera. A digital correlation algorithm was employed to find the vertical displacement field by comparing such refracted images with a reference image corresponding to an undeflected interface. This was followed by a reconstruction of the instantaneous surface height via a numerical integration of the displacement field, a step that leveraged a least square inversion of the gradient operator. This particular re-construction technique provides excellent spatial resolution with good computational efficiency. However, the method returns measurements of limited reliability when the surface curvature is large because it does not utilize collimating optics. This has the advantage of simplicity, certainly, but renders the technique unable to adequately resolve oblique rays, which arise due to strong curvatures. In the present research, because film deflections could have strong curvatures as shown in figure 2.6, it was necessary to adopt an alternative approach capable of measuring A irrespective of the nature of the free surface curvature.

Fourier transform profilometry (FTP) is a popular non-contact 3D measurement technique that has been used in research applications worldwide. In their study of trapped modes in a water wave channel, Cobelli et al. (2009) used FTP to determine the free surface deformation of the local oscillations that occur in water waves propagating through a channel due to a protruding cylindrical obstruction. FTP was also used by Lagubeau et al. (2010) to calculate the free surface deflection of a liquid due to a droplet impact. The working principle of FTP is as follows. Fringes (i.e. Ronchi grating or sinusoidal grating) are projected onto the free surface by a video projector. The image will appear to be distorted when the free surface is deflected. Information pertaining to the free surface topography is thereby encoded in the deformed fringe pattern. It can be decoded by a Fourier transform, filtering in the spatial frequency domain, followed by an inverse Fourier transform (Xianyu and Chen, 2001). The entire free surface can be reconstructed, resolved in space and time. However, and as with the technique discussed in the previous paragraph, this method is most accurate for surfaces with moderate slopes. Therefore for the reasons given above FTP may not represent a suitable technique for the present experiments.

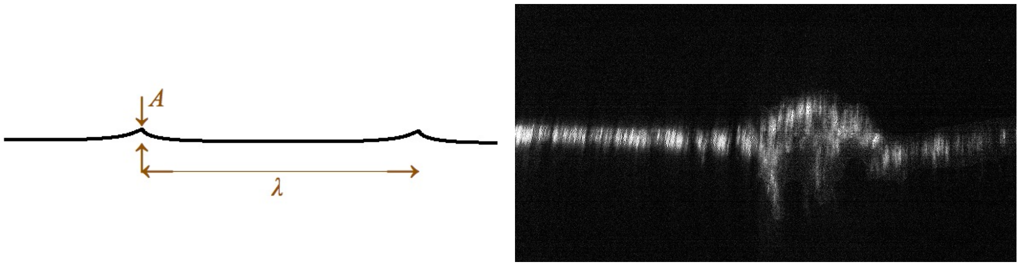

(a) (b)

Figure 2.6: In spite of being in a linear regime, i.e. $A/\lambda \ll 1$, the wave could have a strong curvature. (a) Conceptual sketch of the free surface deflection and (b) actual experimental image.

A PIV technique was considered next. Referring to figure 2.7, the seeding particles, in between successive images, move in both the X-Y plane due to the vertical deflection of the free surface and in the X-Z plane due to the rotation of the disc assembly. The option of a PIV technique based on a single camera was thus eliminated; from a single vantage point, it would be impossible to adequately distinguish between the motion in the X-Y and X-Z planes. Rather a stereo system of the type shown in figure 2.7 is preferred, provided, of course, that deflections in the vertical (Y) direction are no larger than the thickness of the laser sheet. However, a stereo-PIV method requires a complicated setup and calculates the velocity field of the group of particles. We were interested in a comparatively simpler optical arrangement for which measurements of the vertical deflection of the free surface are the only measurements of interest.

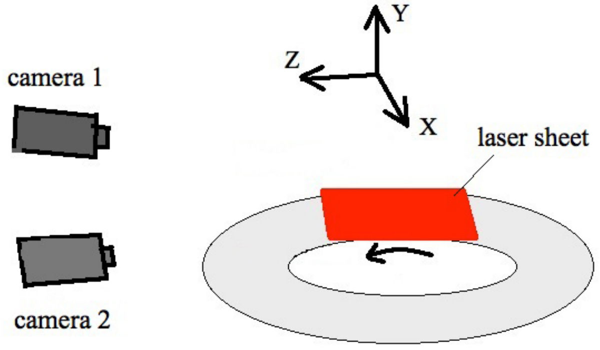

Figure 2.7: Optical set up for a stereo PIV system.

In this vein, we settled ultimately on the optical setup shown schematically in figure 2.8. Our method utilizes a single camera to capture the free surface deflection of a seeded film illuminated by a laser line. Figure 2.8 is only a conceptual schematic; a detailed description of the various components of the system is given in the following subsections.

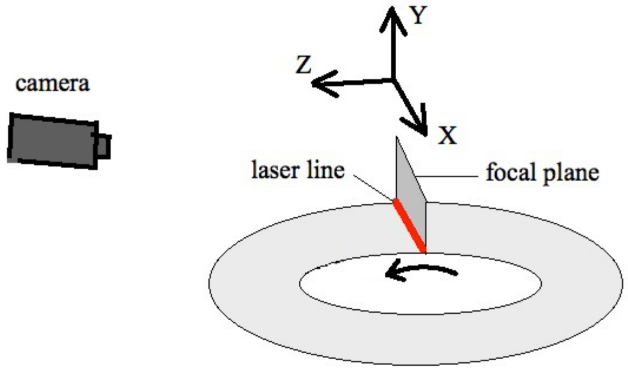

Figure 2.8: Concept behind the optical setup designed for wave amplitude measurements in the present research.

2.2.1 Equipment

The experiments for wave amplitude measurements were performed using both types of silicone oil, i.e. 12,500 cS and 30,000 cS, but only with disc assembly B. When compared to the other disc assemblies, the experiments with disc assembly B generated larger amplitude waves over a wider range of angular speed, which is evident from the data tables A.1 and A.2 of appendix A. Most of the equipment used in the experiments related to the wave amplitude measurements is shared with the experiments described in section 2.1. For example, the glass beaker with all of its contents such as the silicone oil, motors, etc. are the same as mentioned above. Here, and with particular reference to figure 2.9, we focus on the pertinent differences.

The light source is a Cemarline CL 801 manufactured by Cemar Electro Inc. It is a 5 mW class 2 laser pen that emits a line beam of wavelength 670 nm (red light). This particular laser pen was chosen because the light is of approximately uniform intensity along its length. Note that the laser pen was aligned such that the laser line passed through the center of the disc assembly.

The film was seeded with ‘Extendospheres TG Hollow Spheres’ that reflected the laser light, which was, in turn, captured by the camera. The spheres were free flowing and had a diameter range of 10 - 150 μm (with 5 to 10% of the particles being larger than 150 μm according to the manufacturer’s specifications) and a specific gravity range of 0.72 ± 0.05, which makes them lighter than the silicone oil, thereby enabling them to remain at or close to the air-film interface. This was desirable because it allowed the camera to more clearly visualize the reflected laser light.

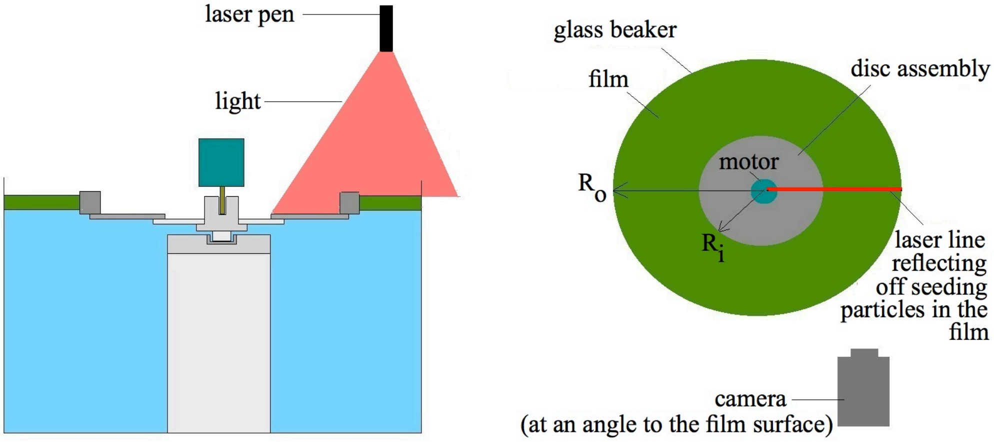

(a) (b)

Figure 2.9: Glass beaker (a) side view and (b) top view.

Upon formation of a wave field as the disc assembly was rotated, the free surface became distorted, and the laser line was therefore deflected upwards and downwards in a time-periodic fashion (figure 2.10). Because the experiments were run in a dark room, the camera saw only the portion of the free surface from which the laser light was reflected in its field of view.

The camera used was a LaVision Imager E-lite with a Nikon 60 mm lens. Each image recorded by the camera was of size 1392 x 808 pixels, which was approximately 26.4 x 15.3 mm in real space. The field of view encompassed the laser line and the edge of the disc assembly, which was marked at regular angular intervals as before for determination of Ω. The camera was kept at an angle of approximately 30^0 with respect to the undisturbed free surface such that it could see the film surface, grazing over the outer wall of the glass beaker.

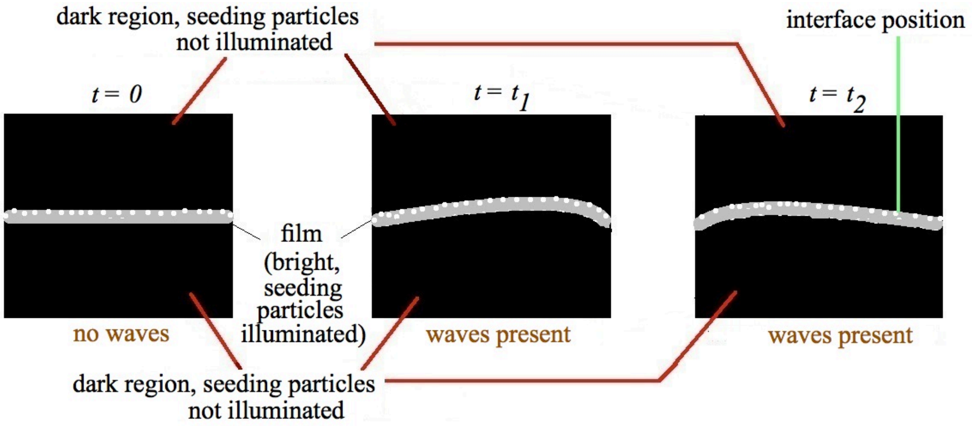

Figure 2.10: The left panel shows a flat laser line when the disc assembly is stationary. The middle panel shows a curved laser line corresponding to the distorted topography of the free surface. The right panel is the same as the middle one, except at a later instant of time when the wave field has moved from its earlier position. Thus, the free surface deflection, as captured by the camera, changes from one image to the next.

Consistent with the discussion of section 2.1.3, the camera frame rate was chosen by balancing illumination and resolution considerations. We ultimately set $f = 15$ fps, which gave adequate temporal resolution and at the same time, kept the interrogation region sufficiently bright.

2.2.2 Experimental procedure

The initial part of the experimental setup, i.e. filling up the beaker with water, setting the disc assembly and motor in place, pouring the oil on top of the water layer, etc. was identical to the description of section 2.1.2.

With the motor rotating slowly, the seeding particles were spread on top of the film by hand. The mass of the viscous oil and seeding particles were each measured using the Acculab balance such that the latter was less than 0.15 % of the former. The concentration was kept low so that the oil properties would remain largely unaltered. For example, according to Einstein's equation (Zhou et al. 2005),

$$\frac{\mu}{\mu_o} = \frac{1}{\left(1 - \frac{\Phi}{\Phi max}\right)^2} \qquad (2.4)$$

where μ_o is the fluid viscosity in the absence of particles, μ is viscosity of the particle-laden fluid and Φ is the particle concentration (mass fraction). Our goal was to remain within a 5% range of the original fluid viscosity, which imposed a maximum value of Φ/Φ_{max} of 2.4%. According to Kamien et al. (2007), the maximum solid volume fraction associated with a random closed packing of spheres is 65%. This translates to $\Phi_{max}= 0.48$ (mass fraction) for the densities considered here and allows a Φ value of upto 0.0114. Thus the quantity of seeding particles added to the film was well within the prescribed tolerance. This is important because, as noted above, we expect most of the particles to congregate near the free surface so that the local value of Φ may in fact be larger than that estimated by the calculation shown in this paragraph. Thus in order to check whether addition of seeding particles affects those parameters we seek to measure, a pair of experiments were performed wherein $m*$ (rather than A) was measured for a film seeded in the manner summarized above. The range of independent parameters was kept as close as possible to a companion set of experiments wherein $m*$ was calculated using a film devoid of seeding particles. In chapter 3 we confirm that the associated measurements of $m*$ are nearly identical between these two experiments.

In each trial, the disc was rotated at two different speeds. The former speed, $\Omega = \Omega_1$, was kept very low such that the film was in motion but no waves could be seen at the free surface, i.e. $0 < \Omega_1 < \Omega_C$, where Ω_C is the critical angular speed associated with buckling onset. The associated experimental images were used in constructing 'base line' images of the type shown schematically in the left panel of figure 2.10. Note that choosing $\Omega_1 > 0$ instead of $\Omega_1 = 0$ ensures a larger seeding particle density in composite images and hence, a smoother and 'fuller' flat line. Here a 'composite image' represents the data from a group of images collected at regular intervals over a certain period of time. Our method for generating a composite image is explained in section 2.2.3 below. The experimental images corresponding to $\Omega = \Omega_1$ were classified as being in a 'no wave region' for the post processing work. Conversely, the latter speed was a larger one in excess of Ω_C, but less than the speed associated with wave breaking, i.e. one for which a regular wave field was observed. The corresponding images were therefore categorized as being in a 'wave region'. By comparing images from the wave and no wave regions, we were able, as explained below, to estimate the wave amplitude, A, for each angular speed, Ω. While keeping the other independent parameters constant, this entire sequence was repeated multiple times by varying Ω giving different data sets classified by the angular speed of the disc assembly. Other precautions such as allowing the oil to rest for at least 30 minutes between trials were followed as in the case of the experiments described in section 2.1.2.

2.2.3 Post processing

This section describes the post-processing techniques employed to obtain the wave amplitude from the image sequence. Figure 2.11 can be used as a 'road map' to guide oneself through the different subsections of 2.2.3.

Visual observation in DaVis and importing the images into MATLAB

The image sequence for each trial was recorded using DaVis 8.0 (by LaVision) operating on a Windows 7 platform. A MATLAB script was written to import the experimental images. Each grayscale image was saved by Davis in .im7 format. In MATLAB, this was read as a structure variable, say '`a`', whose data field, i.e. `a.Data`, represented a 2-dimensional array in which the magnitude of each cell location gave the intensity at the corresponding point in the image. The information was stored in 16-bit integer variables where the lowest value, 0, represented black and the highest value, 65,535, represented white.

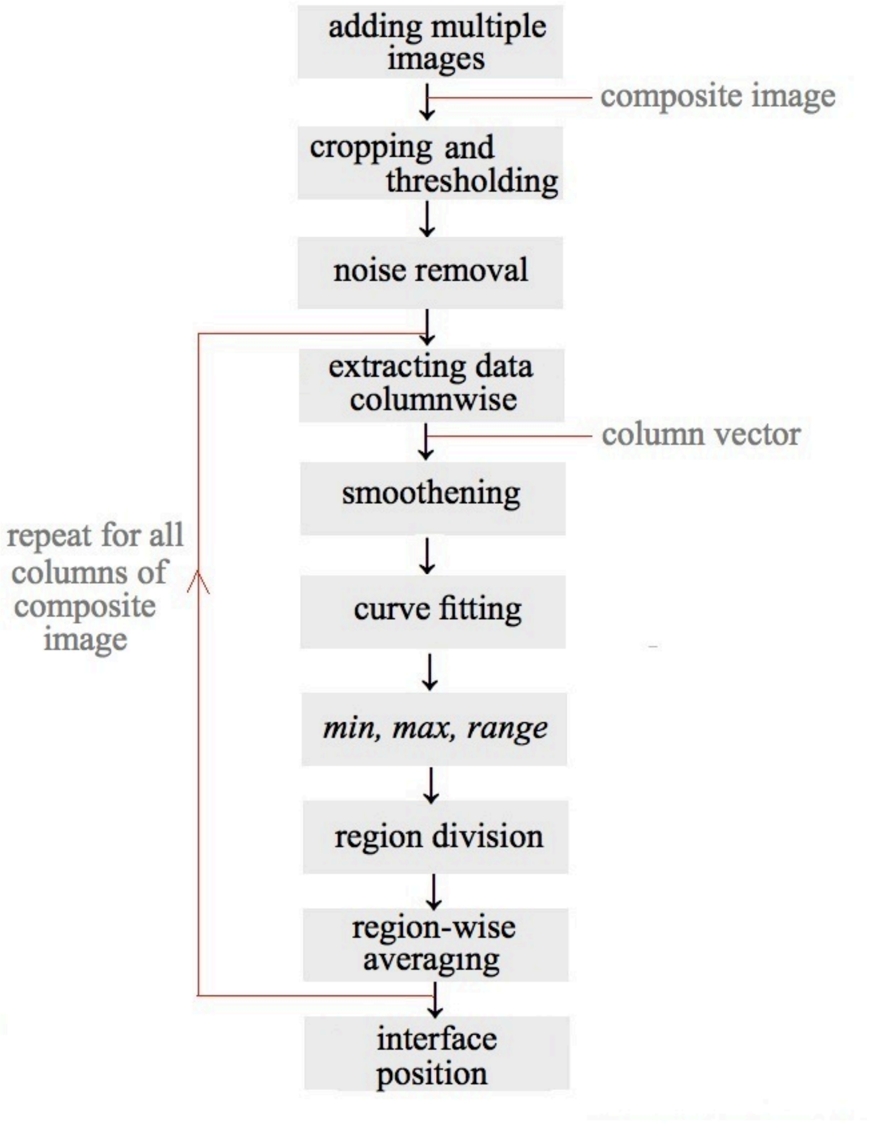

Figure 2.11: Flowchart for the sequence of image processing operations discussed in section 2.2.3.

Note also that, for purposes of being able to convert from pixel space to physical space, one image was recorded under ambient lighting conditions. It had a mm-graded ruler placed in the plane of the laser sheet. This image could be seen directly in MATLAB and a pixel to mm conversion could thereby be made.

The composite image

Instead of sequentially processing each individual image in MATLAB, a group of 25 consecutive images were added together into a single image, henceforth referred to as a ‘composite image’. With a frame rate of 15 fps, each composite image therefore contained information collected over 1.67 s. The image processing was performed on a composite image instead of a single image for the following reasons. Firstly, a single image, as shown schematically in figure 2.12 (a) contains information regarding the distribution of the seeding particles at a single instant in time. Conversely, a composite image, as shown schematically in figure 2.12 (b), containing the collective information of 25 images, records all the seeding particles that passed through the laser line over a longer time interval. This gives many more points per unit area (as shown in the figures below) and therefore a ‘fuller’ region to aid the image processing and interface detection algorithms.

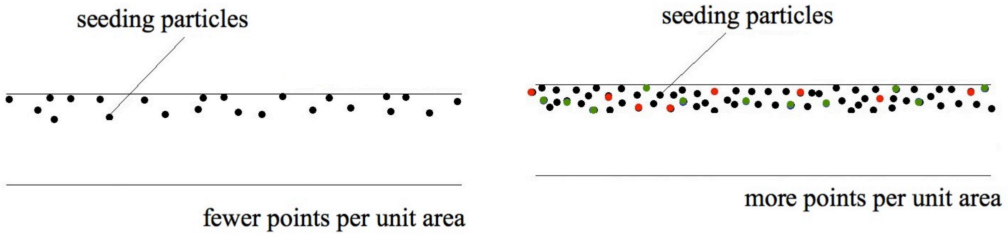

(a) (b)

Figure 2.12: Laser line in (a) a single image and (b) a composite image where the different color dots represent particles observed at different time instants.

Note, moreover, that a composite image may encompass all the different locations of a wave as it translates from the edge of the perimetric ring to the wall of the glass beaker. Waves were observed to change their shape and hence their amplitude as they translated across this field of view. Thus, compared to a single image, the composite image is much more likely to contain information related to the location where the wave reaches its maximum amplitude. This concept is illustrated in figure 2.13.

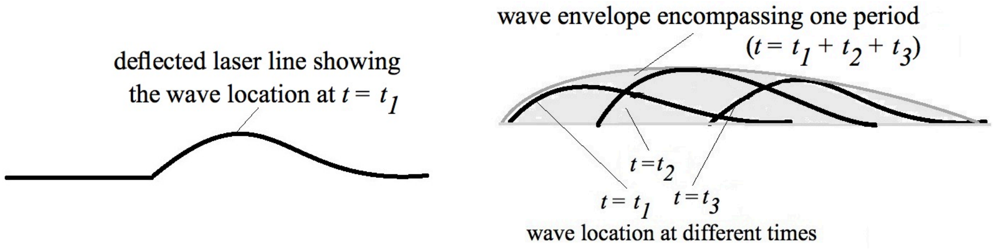

(a) (b)

Figure 2.13: (a) The information contained in a single image recorded at $t = t_1$ and (b) the information contained in a composite image from times $t = t_1$, $t = t_2$ and $t = t_3$; this is similar to the concept of a wave envelope or a wave packet in which the amplitude of the wave envelope is the maximum amplitude of the individual waves (Chapter 9, Kundu, 2008).

Cropping, thresholding and noise removal

A thresholding operation was performed on each composite image to selectively amplify the desired intensity range. Composite images contain data in which the brightest points are less than 10,000 units, which, in a range of 0 to 65,535 is a shade close to black. It is preferable that the brightest points appear as white; so a ‘reference intensity value’, corresponding to the arithmetic average of the maximum intensity values from each individual column, was tabulated. Each composite image was then thresholded such that the pixels having intensities larger than or equal to this reference intensity value were allocated an intensity of 65,535, whereas the darkest pixels were assigned an intensity of 0. The intensity of the intermediate pixels was adjusted accordingly using a linear scale. In other words, the brightest points in the composite image became white whereas the darkest points became black.

Laboratory images were subsequently cropped so as to retain only the necessary information, i.e. that portion of the field of view which showed the waves. This made file sizes smaller, which in turn, increased the run-time efficiency of the MATLAB algorithm.

The algorithm described thus far can be applied to composite images both in the wave and no wave region. In either case we wish ultimately to detect the interface position, which is the curve formed by joining all the pixels that separate the dark region above from the bright region below, i.e. the curve that denotes the air-film interface. We can then compare the results against one another, i.e. by determining the interface position for the wave vs. no wave region to yield an estimate of the wave amplitude for that corresponding angular speed. Figure 2.14 (a) and 2.14 (b) show examples of cropped, thresholded composite images in the no wave region and wave region, respectively. In figure 2.14 (b), the thicker bright region in the center of the image is a hallmark of superposing 25 individual images.

Because the aim is to detect the interface position at the crest of the bright region shown in figure 2.14 (b), the composite images are further cropped row-wise such that the lower boundary of the resultant composite image runs roughly through the middle of the laser line. Rows near the top of the image (figures 2.14a and 2.14b) are also removed so that the resulting cropped image (fig 2.14c and 2.14d) has a smaller dark region above the bright laser line. Henceforth, the phrase ‘composite image’ will refer to a cropped and thresholded image of the type shown in figures 2.14 (c) and 2.14 (d).

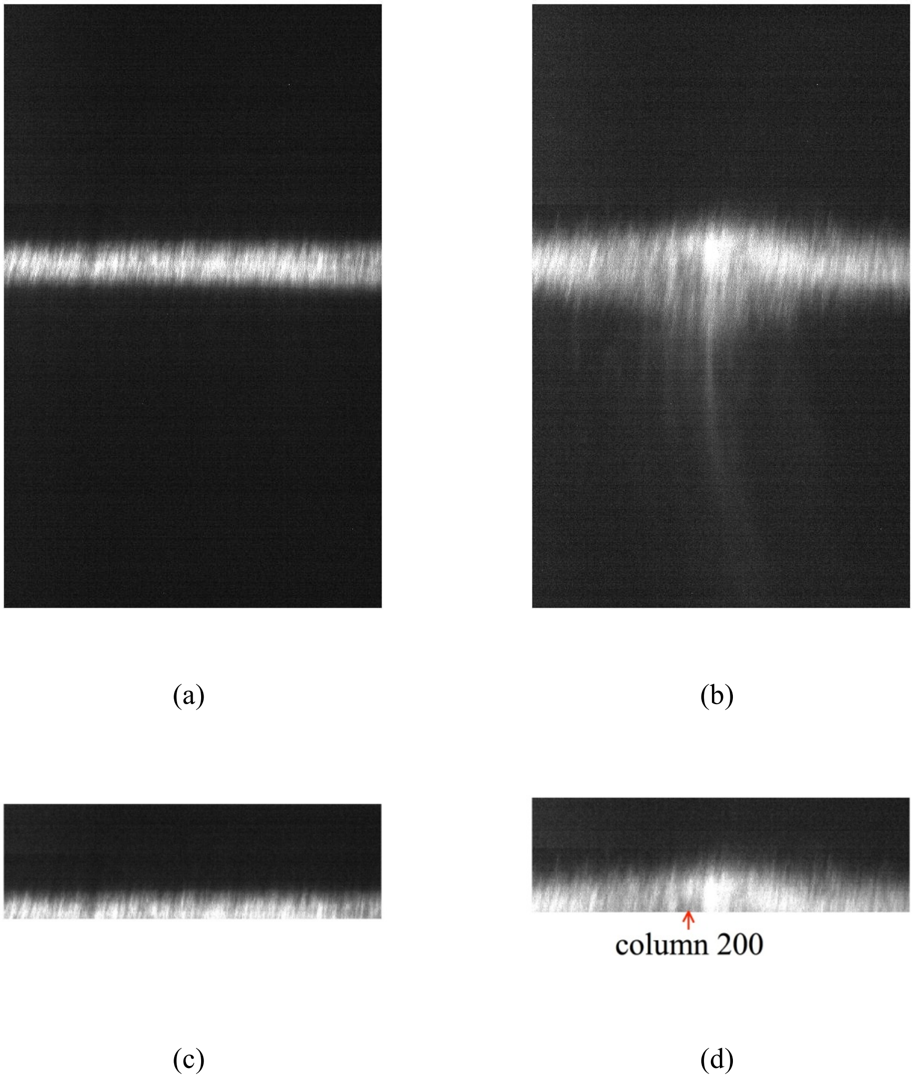

Figure 2.14: Thresholded composite images (a) cropped along the sides, no wave region, (c) same as (a) but cropped along the middle of the laser line, (b) cropped along the sides, wave region, (d) same as (c) but cropped along the middle of the laser line. Figure (a), (b), (c) and (d) correspond to disc assembly B rotating at 2.56 rad/s with 3.15 mm of 12,500 cS oil. Note that figures (a) and (b) measure 15.2 by 9.5 mm (800 by 500 pixels); (c) and (d) are 2.85 by 9.5 mm (150 by 500 pixels). The red arrow in (d) shows column number 200 which is used in figure 2.15.

Finally and so as to minimize experimental noise, each composite image is passed through a median filter. To this end, the MATLAB function '`medfilt2`' was used.

This step reduces the intensity of those pixels whose intensity is significantly different from its neighbours and thereby softens experimental images.

Column-wise processing

The next four paragraphs are dedicated to the processing algorithm that was applied to each column of a composite image. The goal was to determine the interface position by following a one-column-at-a-time, top-down scan approach. The term ‘column vector’ will be used henceforth, which refers to a vertical array that has the intensity values of a particular column of the composite image. Thus figure 2.15 is a top-down intensity plot of the column vector formed from column 200 of 500 of the composite image shown in figure 2.14 (d). The vertical axis denotes the row number and the horizontal axis represents the corresponding intensity values. The green line shows the median-filtered data. This data is passed through a smoothening filter, which eliminates some of the sudden peaks, the result of which is represented by the blue dashed line. For this purpose, the built-in MATLAB function ‘`smooth`’ was employed. Finally a curve fitting approach was applied to the smoothened data and is shown by the red line in figure 2.15. To this end, the built in function ‘`polyfit`’ of MATLAB was applied. Attempts made to directly polyfit the median-filtered data, i.e. eliminating the smoothening stage (since polyfitting is a smoothening operation in its own right), did not yield satisfactory results as small ‘spikes’ were visible in the median-filtered data, which had to be removed for the curve fitting to work properly. The order of the polynomial was chosen to be eight or fifteen for data in the no wave region and wave region, respectively. A larger ‘`polyfit`’ order ensures that the fitted data follows the original data closely; however, it also reduces the efficiency of the MATLAB code. It was found from processing the experimental images that for each case, i.e. the no wave and wave regions, setting the ‘`polyfit`’ order above eight and fifteen, respectively, did not significantly alter the final interface position but did reduce the run-time efficiency of the algorithm. Choosing parameters lower than those specified above, however, had a non-trivial impact on the result which was evidently due to the fact that the fitted data did not follow the original data sufficiently closely.

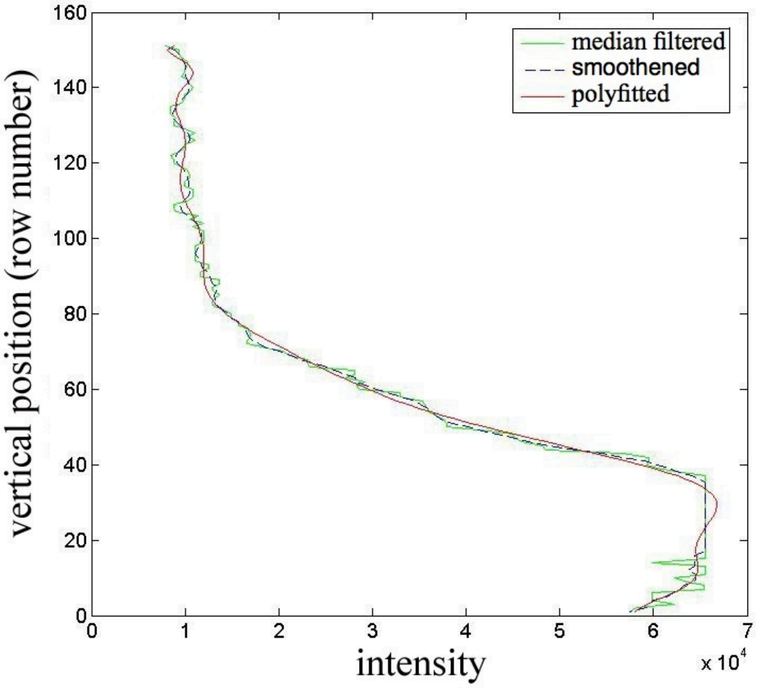

Figure 2.15: Top-down intensity plot of the column vector corresponding to column number 200 of 500 in figure 2.14 (d).

After the curve fitting was completed, the maximum and minimum intensity values of the fitted data were found; these were denoted by *min* and *max,* respectively. The difference between *max* and *min* was called the *range*. The column vector was divided into three distinct zones: a dark zone (the region of low pixel intensity that is above the reflected laser line), a bright zone (the region of high pixel intensity coinciding with the reflected laser line) and a transition zone (the region of intermediate intensity in between the two aforementioned zones). Scanning the column vector top-down, the algorithm searches for the row value, furthermost from the top, where the fitted data surpasses an intensity value of *min* + 0.2 *range*. We consider the associated row value as the lower boundary for the dark zone. The algorithm also finds the row value, closest to the top, where the fitted data surpasses an intensity value of *min* + 0.8 *range*, i.e. *max* - 0.2 *range*. This row value is considered to be the upper boundary of the bright zone.

As illustrated in figure 2.16, the transition zone is defined as the region falling between these upper and lower boundaries. Note that consistent with the profile of figure 2.14 (d), the lower and upper boundaries of this transition zone are not fixed but vary slightly as we move from one column to the next.

It is important to emphasize that the factor of 0.2 from the previous paragraph was not selected arbitrarily. Choosing a value lower than 0.2 (say 0.1) resulted in the transition region engulfing the portion of the column vector where the intensity was very low (or very high for the *bright* region) i.e. where the intensity curve changed directions frequently. On the other hand, selecting values larger than 0.2 resulted in the transition region becoming narrower as the dark and bright regions occupied a larger portion of the column vector. This shifted the average intensities of the dark and bright zones in opposite directions but did not significantly influence our final estimate for the interface position.

Mean intensities of the dark zone and the bright zone are denoted, respectively, by I_d and I_b and are determined from the filtered column vector data. The arithmetic mean of I_d and I_b, I, represents the intensity at a point in the transition zone which we assume to correspond to the interface position. Thus the row value where the intensity of the polyfitted data coincides with I is deemed to represent the interface position for that column of the composite image. Repeating this process, all the individual column-specific interface position values were mapped on top of the composite image as shown in figure 2.17. Thus the interface position across the entire composite image was computed.

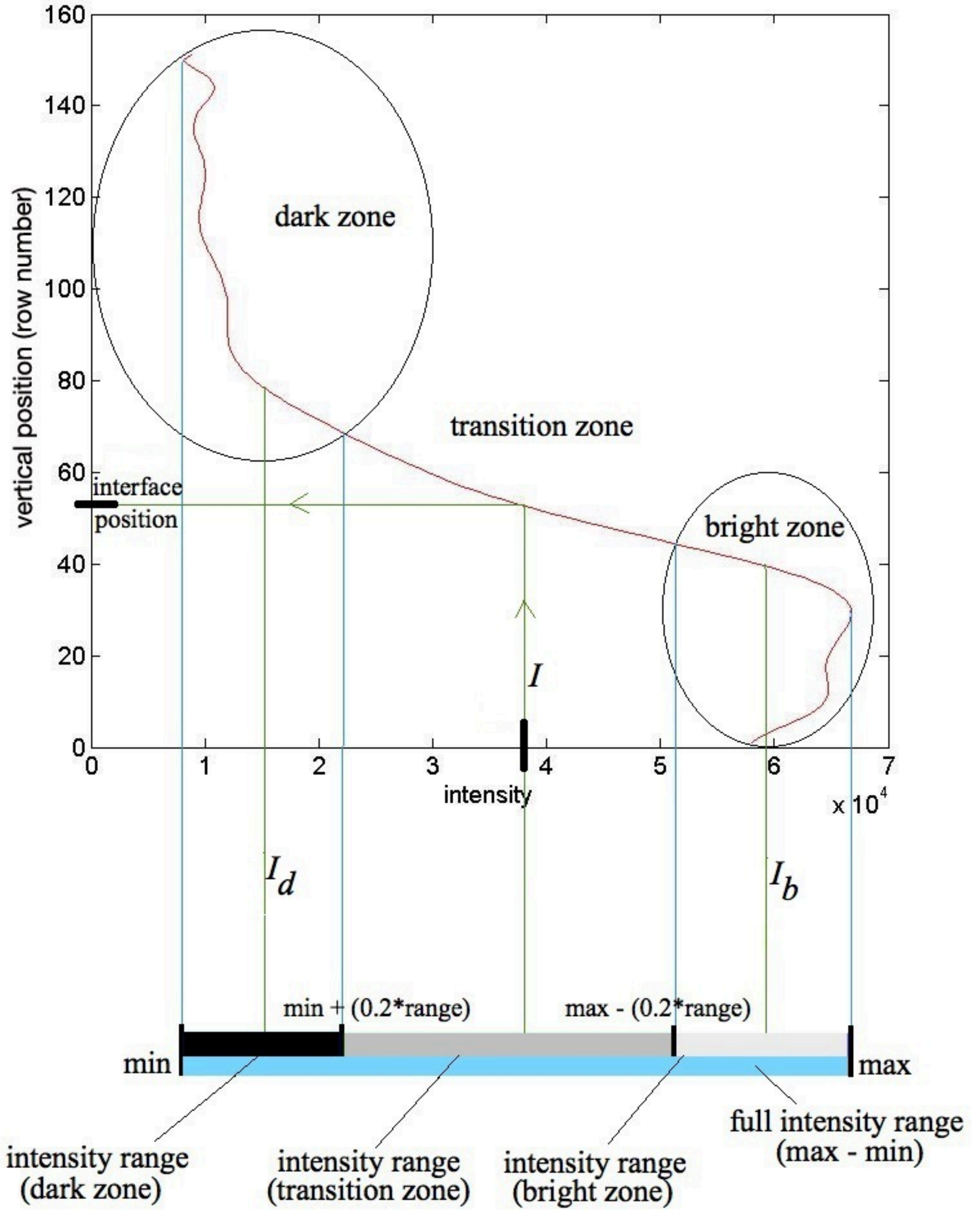

Figure 2.16: Schematic showing how the column vector was divided into separate zones and how the interface position was detected.

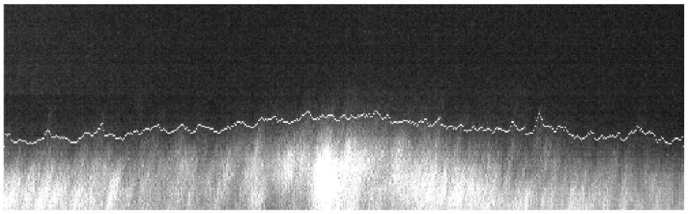

Figure 2.17: Laboratory image showing the interface position as computed using the image processing algorithm of section 2.2.3 superposed on top of the experimental image of figure 2.14 (d).

Final wave amplitude

The image processing routine described above, detects the interface position in a single composite image. The peak value of the interface position for the composite image is denoted by A_1. A baseline composite image, corresponding to 25 images in the no wave region was also processed. The average value of the interface position for the baseline composite image was denoted by A_0. The wave amplitude, in pixels, was the difference between A_1 and A_0. However, as noted above, for a fixed angular speed, Ω, multiple composite images were processed. An average of the wave amplitude values for different composite images (for the same Ω) gave the final wave amplitude, A, for that particular Ω. This wave amplitude (in pixels) was multiplied by a calibration factor derived from the aforementioned calibration image to give the wave amplitude in mm rather than in pixels.

Note that the MATLAB script that performs the operations described in section 2.2.3 is presented in Appendix E.

Validation

This paragraph focuses on the validation of the experimental and post processing techniques employed for the wave amplitude measurements. A metal sphere having a diameter of 3.04 mm, measured using a vernier caliper, was placed on top of the perimetric ring of disc assembly B. The camera, located in the same position as before, captured the deflection of the laser line reflecting from the top surface of the metal sphere as the disc assembly was rotated. Experimental images were processed using the same MATLAB algorithm as discussed above. The difference of the interface position between the top of the metal sphere and that of the top edge of the perimetric ring was determined. A similar calibration method as discussed above yielded a diameter measurement of 2.89 mm. This introduces an error of less than 5% when compared to the actual dimensions of the sphere. Note that in performing this calibration experiment, all experimental parameters, most significantly the object distance, was kept as close as possible to the thin film experiments discussed previously.

2.3 Sinuous vs varicose waves

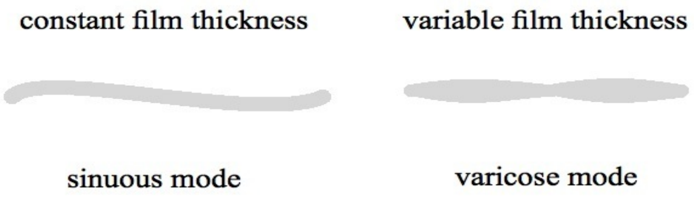

Figure 2.18: Sinuous vs. Varicose modes

The analysis of section 2.2 provides a means of estimating the deflection of the free surface, however, it cannot readily be extended to compute the deflection of the internal (i.e. film–water) interface. In this respect, it should be recalled that the wave forms associated with ‘thin’ geometries such as thin films and filaments can be broadly divided into two groups. As shown in figure 2.18, in a sinuous mode, the two opposite surfaces are parallel to each other and follow the center-line of the film. A varicose mode resembles a ‘pinch-and-swell’ structure so that the film thickness varies with the horizontal coordinate in a periodic fashion. Although there can be a wave form in between these two archtypes, consideration of such cases is beyond the scope of the present discussion. As mentioned previously, the theoretical model in chapter 1 assumes that the wave field is sinuous.

Although a method based on light attenuation for determining whether the wave field is sinuous or varicose was considered, due to the technical difficulties listed below, it could not be satisfactorily implemented in the laboratory. When the film is illuminated from below as in figure 2.2, the recorded images will exhibit a spatially variable intensity if the film is of non-uniform thickness. Thus the intensity might be expected to be uniform for a sinuous mode because the film thickness is constant but not so in the case of varicose mode. However, a more careful investigation reveals a flaw with this argument. As noted in section 2.1.3, there are other factors that also affect the intensity of an image such as the slope of the free surface. Thus a method based on light attenuation, is not a conclusive test of determining whether the film is of variable thickness. Intrusive methods were not considered because contact with an external object would change the shape of the free surface.

Chapter 3 - Results and discussion

In this chapter, results are presented and analyzed. The former part deals with the results of the wave count and relative speed experiments and the latter part shows the results from the wave amplitude experiments. The complete data set showing all the data collected in the laboratory is presented in a tabular form in Appendices A and B.

3.1 Wave count and relative speed

Each figure in this section shows data obtained from multiple trials of a particular experimental setup, i.e. Ω varies but h, R_i and ν remain constant. Further, each figure is comprised of two subplots. That on the left shows the variation of m^* and that on the right shows the variation of C_p/Ω. In all cases, the horizontal axis gives a non-dimensional angular speed, ΩT. The plots for m^* vs. ΩT, in addition to representing the experimental data points also show predictions of the theoretical model, which is obtained by solving (1.9). By comparing the two data sets, we may assess the accuracy of the theoretical model, which is one of the primary objectives of this thesis and the companion manuscript Bhattacharya, Craster and Flynn (2012).

The figures presented below have been arranged in ascending order of film viscosity, then in ascending order of disc assembly radius and finally in ascending order of film thickness. The vertical line drawn near the bottom left corner of each plot is an average error bar for the associated experimental data points.

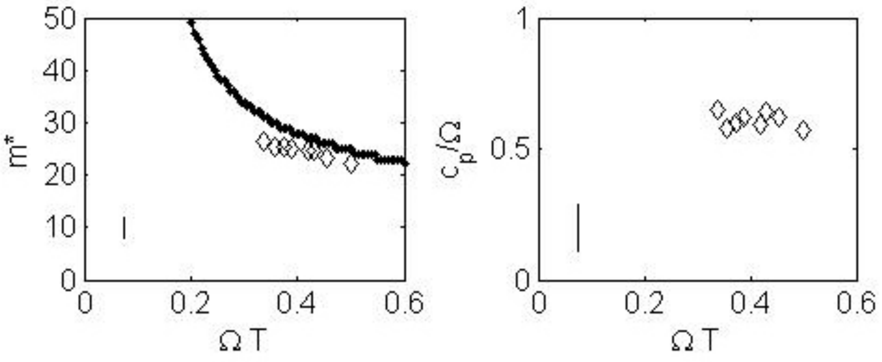

(a) (b)

Figure 3.1: Comparison between the solution of (1.9) and experimental data for ε = 0.0160, Υ_1 = 14.5, $\Upsilon_2 = 4.50 \times 10^{-3}$ (i.e. ν = 12,500 cS) and β = 0.497 (i.e. disk assembly A). Note that the experimental data is an amalgam of three independent trials with ε = 0.0150, ε = 0.0163 and ε = 0.0165 (i.e. film thicknesses 2.20, 2.40 and 2.42 mm). Representative vertical error bars are as indicated. The hollow points represent the experimental data whereas the solid points correspond to the theoretical predictions. The variables Υ_1 and Υ_2 are been defined by (1.11).

Figures 3.1 to 3.5 show the results for the lower viscosity oil. As a general trend, it can be seen that, with some fluctuations, m^* decreases with Ω whereas C_p/Ω remains bounded in the 50 - 65 % range, which is in good agreement with the findings of Suleiman and Munson (1981) who reported $C_p \sim 0.5\Omega$. In all cases, the theoretical prediction of m^* satisfactorily agrees with the corresponding experimental results, particularly for small Ω. For all the data presented in section 3.1, the experimental points typically deviate from their theoretical counterparts by only 10 - 15% and the discrepancy never exceeds 25%.

In figures 3.1 to 3.9, the theoretical values of m^* are integer numbers, and hence the curve for the theoretical predictions takes the form of a 'staircase' instead of a smooth curve. Conversely, each experimental data point for m^* is a result averaged over multiple image pairs for that particular Ω and can therefore be a real number.

Consistent with the discussion of chapter 2, measurements of *m** are presented only for those Ω where a regular wave field was observed. As is evident from figures 3.1 and 3.2, and, more especially, figures 3.3 and 3.4, this interval shifts towards higher angular speeds with an increase in the film thickness, for fixed β. A corresponding decrease in *m** is associated with this shift. The disc assembly C has a larger perimeter when compared to that of A and B, by a factor of 1.7 and 1.25, respectively. This difference in size could help to explain the reason behind the larger *m** values observed in figure 3.5 (disc assembly C) when compared to figures 3.1 through 3.4 (disc assemblies A and B).

As discussed in chapter 2, a separate set of experiments was performed to investigate the effect of adding seeding particles to the film. Note that figure 3.3 and 3.4 show the variation of *m** and C_p/Ω with ΩT for a seeded film (stars) as well as an unseeded film (open diamonds). Special care was taken to ensure that the range of independent parameters was as close as possible to the original experiments so that the results can be meaningfully compared. In this vein figures 3.3 and 3.4 imply that there is no significant variation of *m** or C_p/Ω due to seeding, not at least for the low seeding concentrations used here.

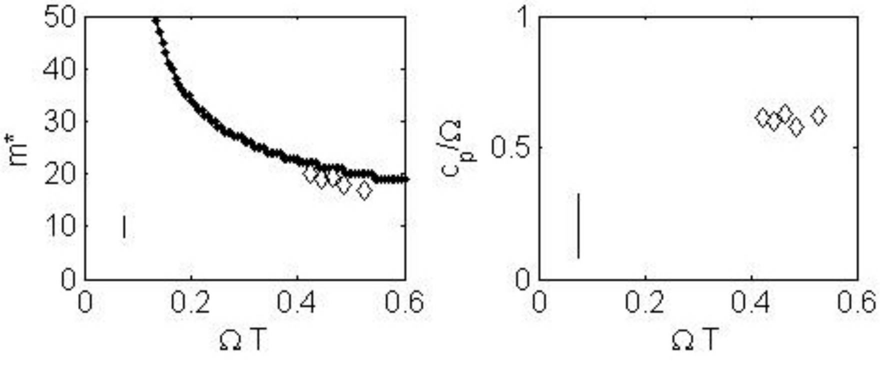

(a) (b)

Figure 3.2: As in figure 3.1 but with ε = 0.0238 (i.e. a film thickness of 3.5 mm).

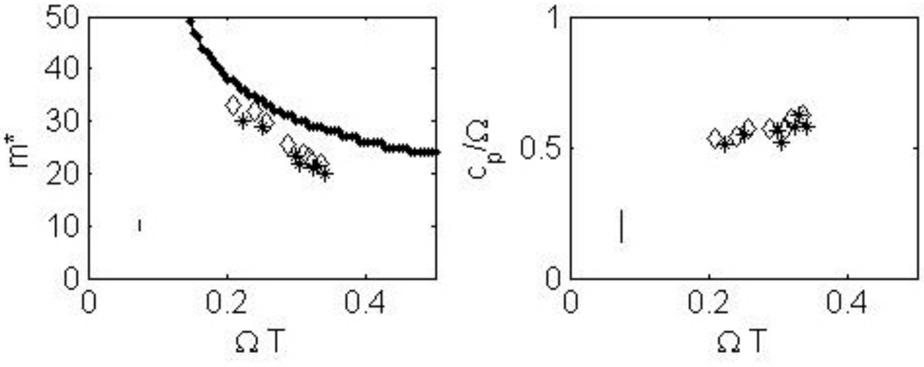

(a) (b)

Figure 3.3: As in figure 3.1 but with ε = 0.0199 and β = 0.667 (i.e. disk assembly B). Note that the open diamonds correspond to experimental data which is an amalgam of two independent trials with ε = 0.0193 and ε = 0.0209 (i.e. film thicknesses 2.84 and 3.07 mm) and the stars correspond to experimental data wherein the film was seeded with spherical hollow spheres, and corresponds to ε = 0.0205 (i.e. a film thickness of 3.01 mm).

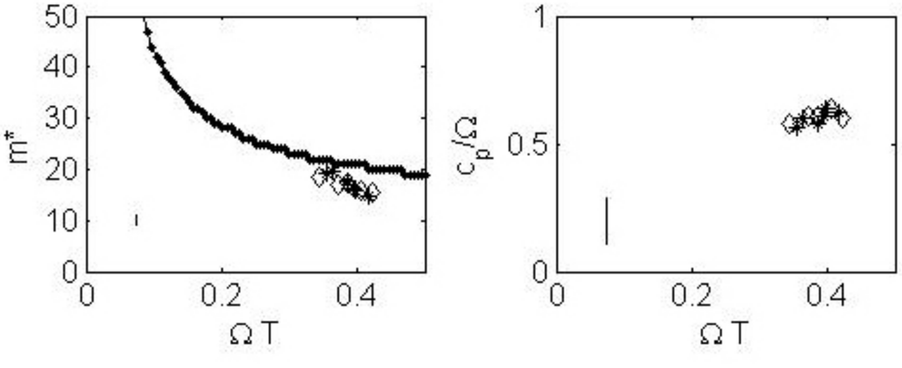

(a) (b)

Figure 3.4: As in figure 3.3 but with ε = 0.0337 (i.e. a film thickness of 4.95 mm) for the unseeded film (open diamonds) and ε = 0.0331 (i.e. a film thickness of 4.86 mm) for the seeded film (stars).

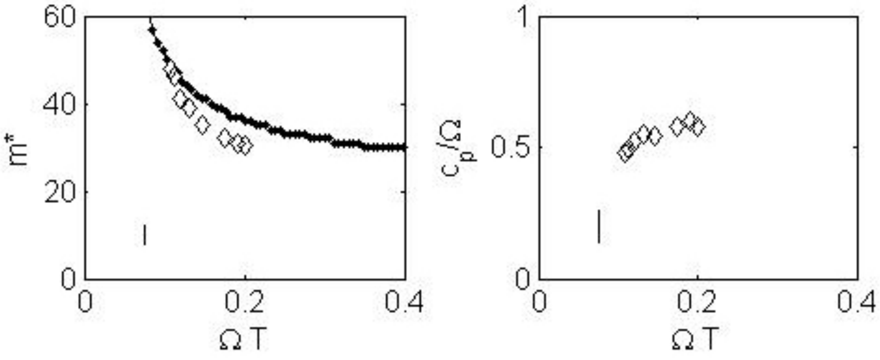

(a) (b)

Figure 3.5: As in figure 3.1 but with ε = 0.0186 and β = 0.844 (i.e. disk assembly C). Note that the experimental data is an amalgam of three independent trials with ε = 0.0182, ε = 0.0188 and ε = 0.0191 (i.e. film thicknesses 2.68, 2.77 and 2.81 mm).

Figures 3.6 to 3.9 show comparable results but correspond to the higher viscosity oil. Supplementing the previous discussion, it can be seen that the interval in which a regular wave field is realized occurs at much lower values of angular speed for the 30,000 cS oil as compared to the 12,500 cS oil. As noted by Suleiman and Munson (1981), the critical shear stress is proportional to the product of film viscosity and velocity, and is nearly constant for $h/(R_o - R_i) < 0.2$, a geometric criterion that is satisfied for the experiments presented in this thesis. Thus, assuming that approximately the same critical shear stress is required to buckle either film, the instability threshold is expected to coincide with lower angular speeds for the 30,000 cS film when compared to the 12,500 cS film. A further difference between the 12,500 cS and 30,000 cS films is that in the latter case, the angular speed at which the waves begin to break is closer to the threshold angular speed. Thus when compared to the lower viscosity oil, the interval corresponding to a regular wave field is notably narrower in the 30,000 cS case.

Unlike all the other cases where the experimental values of m^* are close to or below their theoretical counterparts, in figure 3.7 (a) it can be observed that the experimental values of m^* universally lie above the theoretical predictions. The reasons underlying this observation are not immediately obvious but form an interesting point for further study.

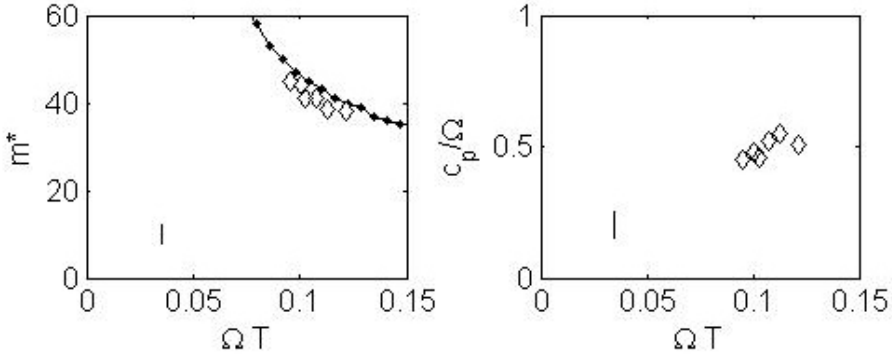

(a) (b)

Figure 3.6: Comparison between the solution of (1.9) and experimental data for $\epsilon = 0.0130$ (i.e. a film thickness of 1.91 mm), $\Upsilon_1 = 6.05$, $\Upsilon_2 = 1.88 \times 10^{-3}$ (i.e. $\nu = 30{,}000$ cS) and $\beta = 0.667$ (i.e. disk assembly B).

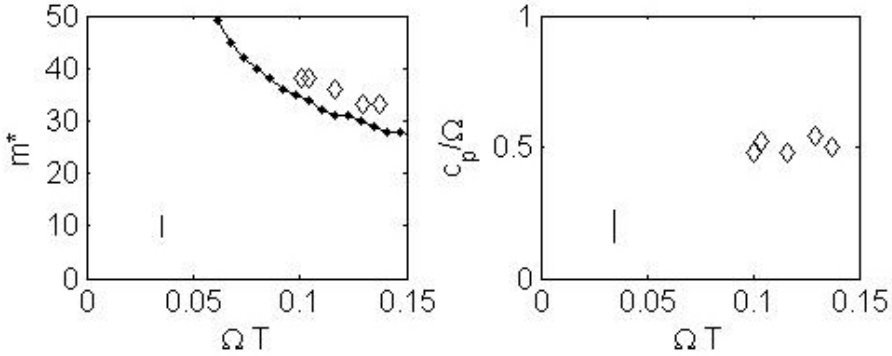

(a) (b)

Figure 3.7: As in figure 3.6 but with $\epsilon = 0.0201$ (i.e. a film thickness of 2.95 mm).

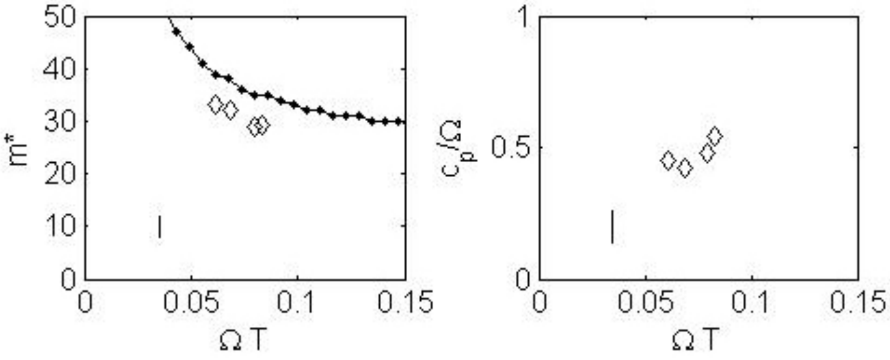

(a) (b)

Figure 3.8: As in figure 3.6 but with ε = 0.0208 (i.e. a film thickness of 3.05 mm) and β = 0.844 (i.e. disk assembly C).

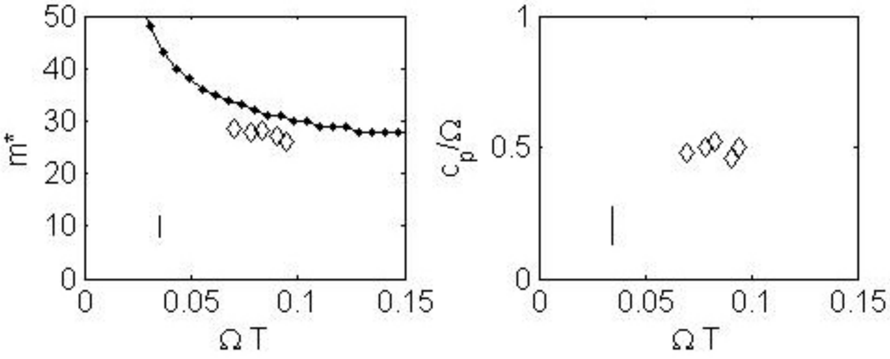

(a) (b)

Figure 3.9: As in figure 3.8 but with ε = 0.0283 (i.e. a film thickness 4.16 mm).

Note finally that the largest ($m^*_{\text{max}} = 48.0$) and smallest ($m^*_{\text{min}} = 15.4$) number of waves measured using the present apparatus correspond to the following respective sets of experimental parameters: relatively thin film ($\varepsilon = 0.0186$) with disc assembly C at a comparatively low angular speed of 0.88 rad/s ($\Omega T = 0.108$);

and a relatively thick film ($\varepsilon = 0.0337$) with disc assembly B at a comparatively large angular speed of 3.45 rad/s ($\Omega T = 0.422$). In both cases, $\nu = 12{,}500$ cS.

When contrasted with figure 3.5 (a) of Teichman (2002), where the experimental and theoretical values of the wave count are in good agreement for $\beta < 0.2$ but deviate from one another by about a factor of about two thereafter, there is a very positive agreement between theory and experiment over the entire range of independent parameters in our work. This difference may be attributed to one or more of the following reasons. Present-day state-of-the-art flow visualization hardware and software has been used in the present research. By contrast, Teichman's experiments were conducted no later than 2002. Also, a number of equations in Teichman's work, such as his (3.15) and (F.3) contain typos; it is uncertain if these were introduced while typesetting or at an earlier derivational stage. Finally, and as described in chapter 1, Teichman used a less precise set of characteristic variables when non-dimensionalizing his equations, e.g. his (2.7). Here by contrast the definitions of the scaling variables are unambiguous; horizontal lengths were scaled with the outer radius R_o and vertical lengths with the film thickness h.

3.2 Wave amplitude

We turn now to the wave amplitude measurements. Keeping all other independent parameters constant, the angular speed was again varied between different trials as described in chapter 2. The variation of the wave amplitude, A, with the angular speed, Ω, is of primary interest here.

In figures 3.10 and 3.11, A, has been divided by h to non-dimensionalize the vertical axis and Ω has again been multiplied by T to non-dimensionalize the horizontal axis. Each figure corresponds to a particular oil viscosity and contains data points for two different values of h with open and closed circles, giving the smaller and larger layer thicknesses, respectively. The vertical dotted and solid lines specify, respectively, a representative error bar for the open and closed data points. Error bars are based on the mean difference between the maximum and minimum measured value of *A* for all those data points that fall outside the region of bistability, which we describe in more detail below. Note that all the data points shown in figures 3.10 and 3.11 correspond to a regular wave field in the sense that the spacing between adjacent wave crests was approximately constant.

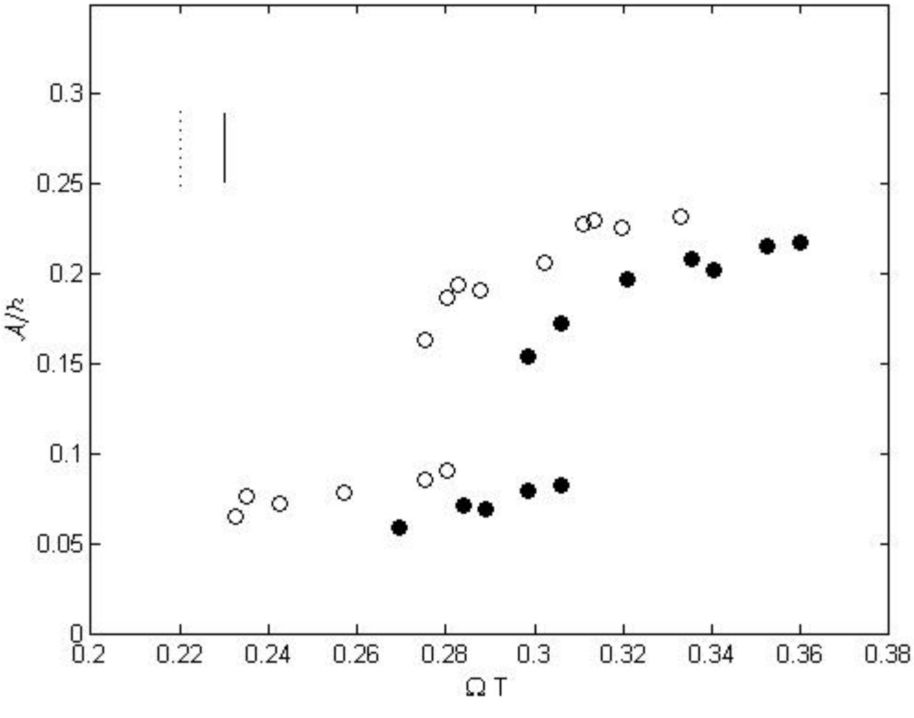

Figure 3.10: One half of the peak-to-peak wave amplitude (normalized by the film thickness, *h*) vs. the non-dimensional angular speed ΩT corresponding to Υ_1 = 14.5, Υ_2 = 4.50×10^{-3} (i.e. ν = 12,500 cS) with β = 0.667 (i.e. disc assembly B). The open and closed circles correspond to ε = 0.0214 (*h* = 3.15 mm) and ε = 0.0269 (*h* = 3.96 mm), respectively.

Figure 3.10 shows the variation of A/h for the lower viscosity oil. Consider first of all the open circles with $\Omega T \leq 0.26$. Here A/h is quite small and nearly constant, being less than 0.08. Conversely, for $\Omega T > 0.28$, large amplitude waves with $0.19 \leq A/h \leq 0.23$ are found. Similar behavior can also be seen for the thicker film with smaller wave amplitudes corresponding to $\Omega T < 0.29$ and notably larger wave amplitudes for $\Omega T > 0.32$. In either case, there is a narrow band of angular speeds, referred as the region of bistability, where both small as well as large amplitude waves were recorded in the same trial, i.e. for fixed Ω. In studying the buckling of a rectilinear elastic plate, Balmforth et al. (2008) mention a similar region of bistability; however, there are prominent differences. Namely, in Balmforth et al.'s study, sudden changes in the out-of-plane displacements are simultaneously accompanied by variations in the planar expanse of a wrinkle. Conversely, and although we cannot simultaneously measure m^* and A, a different behavior is believed to occur here. Consider for example figures 3.3 and 3.10. The open circles of figure 3.10 share similar independent parameters to the open diamonds of figure 3.3, i.e. disc assembly B, comparable film thicknesses and identical film viscosity. Although a jump in A is seen at approximately $\Omega T = 0.28$ in figure 3.10, no such sudden change in m^* is apparent in figure 3.3. Making a conclusive remark regarding this difference in behavior between A and m^* for a viscous film would require further investigations in which simultaneous measurements of A and m^* were made.

Note finally that, in addition to figures 3.1 to 3.9, figure 3.10 provides further evidence that the interval of ΩT in which a regular wave field occurs shifts towards larger angular speeds as the film thickness is increased. A possible explanation is that the buckling resistance term of (1.9) is proportional to h^3 and thus it is easier to buckle a thin film compared to a thick one.

Figure 3.11 is similar to figure 3.10, but shows the wave amplitude data for the higher viscosity oil. As in figure 3.10, there is a narrow band of angular speeds where small as well as large waves are observed in the same experimental run.

These points occur at $\Omega T = 0.093$ for the thinner film and between approximately $\Omega T = 0.103$ and $\Omega T = 0.107$ for the thicker film. Unlike figure 3.10, where A remained relatively small for a certain range of very low angular speeds but became notably larger thereafter, in figure 3.11, there is no interval of ΩT where only small amplitude waves were detected.

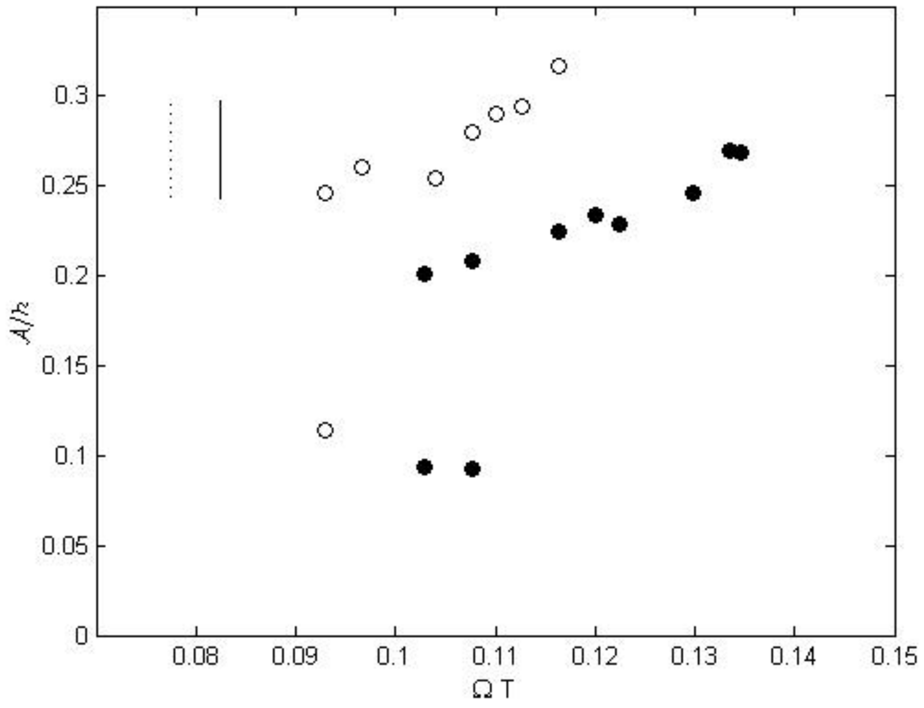

Figure 3.11: One half of the peak-to-peak wave amplitude (normalized by the film thickness, h) vs. the non-dimensional angular speed ΩT corresponding to $\Upsilon_1 = 6.05$, $\Upsilon_2 = 1.88 \times 10^{-3}$ (i.e. $\nu = 30{,}000$ cS) with $\beta = 0.667$ (i.e. disc assembly B). The open and closed circles correspond to $\varepsilon = 0.0139$ ($h = 2.04$ mm) and $\varepsilon = 0.0205$ ($h = 3.01$ mm), respectively.

Consistent with the discussion in section 49.1, of Drazin and Reid (1981), *A/h* typically increases with ΩT, though not in a linear fashion. A rudimentary model describing the non-linear growth of perturbations was proposed by Landau in 1944 (Drazin and Reid, chapter 7, 1981) according to which the perturbation amplitude, A, evolves in time as

$$\frac{\mathrm{d}|A|^2}{\mathrm{dt}} = 2\sigma|A|^2 - l|A|^4 \tag{3.1}$$

Here l is the Landau constant and σ is the growth rate. Landau's model yields a 'pitch-fork' bifurcation as shown schematically in figure 3.12. There is experimental evidence that elastic membranes deform as described by Landau's model. More specifically, Geminard et al. (2004) showed the variation of amplitude (and wavelength) in a thin elastic membrane as it is subjected to an axisymmetric tensile force. They demonstrated (their figure 8) that the wrinkles appeared only after a certain threshold forcing was surpassed. Upon increasing the forcing beyond that critical point, the amplitude increased in a manner consistent with the curve of figure 3.12. However, as shown in figures 3.10 and 3.11 a pitch-fork type variation of A/h with ΩT is not observed in the present context. This may be added as a further dissimilarity between the behavior of viscous films and elastic membranes.

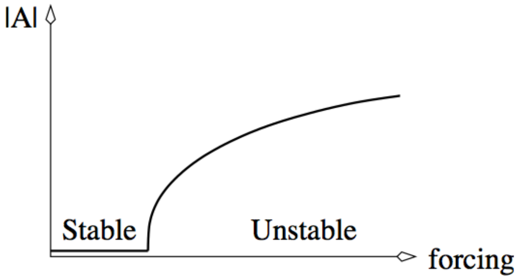

Figure 3.12: A 'pitch fork' bifurcation showing the variation of wave amplitude with the applied forcing, adapted from Drazin and Reid (figure 1.7a).

Chapter 4 - Conclusions

In this chapter, an overall summary of the research work is presented. Some applications that may benefit from this research are also identified. The chapter ends by looking at the possibilities for extending the present research.

4.1 Summary of the present contribution

As suggested by the title of the thesis, in this research, the buckling response of a thin film of viscous liquid, subjected to planar shear in an axisymmetric geometry was studied; to this end, experimental methods and post-processing techniques were utilized. The domain of interest of the present research is in the analysis of the out-of-plane deformation of a thin horizontal film. Our work thereby builds on the experimental and/or theoretical observations of Taylor (1969), Suleiman and Munson (1981), Benjamin and Mullin (1988) and Teichman (2002), all of whom considered a similar problem and flow geometry

The details of our experimental procedure are as follows: thin films of silicone oil having viscosities of 12,500 or 30,000 cS and thicknesses between 1.95 and 4.95 mm floated on top of a much deeper layer of water and were laterally constrained by cylindrical surfaces consisting of a fixed outer boundary and a rotating inner one. This rotation gave rise to a velocity gradient in the horizontal film, which, coupled with the high viscosity of the silicone oil, yielded large in-plane shear forces. The film surface remained undisturbed when the rotation rate was low. Conversely, for higher values of Ω, wrinkles were observed in the film. The independent parameters were (i) the film viscosity, ν, (ii) the film thickness, h, (iii) the non-dimensional disc assembly radius R_i/R_o and (iv) the angular speed, Ω.

Using indigenously designed optical setups, the data was captured only in a region where the wave-field appeared to be regular with an approximately uniform spacing between successive wave crests. This region of a regular wave field occurred over different intervals of Ω depending on the values of the other independent parameters. The experimental images were processed in MATLAB using the image processing toolbox to obtain the dependent parameters: (i) the azimuthal wave number, m^*, (ii) the relative speed, C_p/Ω (ratio of the phase speed of the waves to the angular speed of the disc assembly) and (iii) the wave amplitude, A.

According to the Stokes-Rayleigh analogy, when subjected to shear, thin viscous films exhibit similar behavior when compared to thin elastic membranes. Citing the Stokes-Rayleigh analogy, Slim et al. (2012) remark "there is a close connection between the governing equations for elastic and viscous plates as well as between the associated buckling instabilities." In the light of this analogy, the Foppl von Karman equation, which have more traditionally been used to describe the wrinkling of elastic membranes (Landau & Lifshitz 1986; Coman & Bassom 2007), has been adapted to study the fluidic problem (Taylor, 1969 and Teichman, 2002). Although this thesis principally considers experimental measurements of m^*, C_p/Ω and A, an outline of the theoretical model based on the fluidic version of the Foppl von Karman equation is also presented for completeness. Figures 3.1 through 3.9 show the variation of m^* with the non-dimensional angular speed ΩT where both experimental results as well as model predictions are presented. The experimental results agree well with the theoretical predictions, which demonstrates not only the effectiveness of the model based on the fluidic version of the Foppl von Karman equations, but, more generally, the validity of the Stokes Rayleigh analogy. Note, however, that there are limitations to the range of the experimental data as well as the parameter space of the theoretical model. More specifically and in the latter case, degeneracies arise if any of Ω, h or the gap width becomes very small. Although these shortcomings, first identified by Benjamin and Mullin (1988), are non-trivial, it should also be noted that $\Omega T \rightarrow 0$

signifies that $m^* \rightarrow \infty$ and $\sigma \rightarrow 0$. Thus the perturbations are expected to grow indefinitely slowly so that equations such as (2.10) can be more useful than suggested by Benjamin and Mullin's criticisms.

The agreement between experiment and theory for the values of m^* in the present research is notably better than that achieved by Teichman (2002). The theory, however, cannot predict C_p or A. It is observed experimentally that the phase speed of the waves is between 50 – 65% of the angular speed of the disc assembly, which is in good agreement with the findings of a previous investigation by Suleiman and Munson (1981). To the best of our knowledge, estimates of the wave amplitude have not been previously reported for an experiment of the kind considered here. The wave amplitude data, as presented in figures 3.10 and 3.11, shows that A/h increases with ΩT and also reveals a limited region of bistability where waves of small or large amplitude are excited at the same value of Ω.

Various examples of viscous buckling were presented in chapter 1 which included lava flows and batter poured into a pan. Marine oil spills, where a thin film of oil floats atop a much deeper layer of ocean, were also discussed to highlight the effect of shear on film stability and also to emphasize the need for a better understanding of the mechanical response of a film to an applied force or forces to help in improving remediation strategies. As highlighted in section 1.2, the theoretical equations were non-dimensionalized by selecting appropriate length scales, as a result of which, the non-dimensional variables β (geometry), ε (film thickness), Υ_1 (associated with gravity), Υ_2 (corresponding to surface tension) were introduced. This is especially important in light of the application and adaptability of these equations to scenarios outside of the present laboratory experiments. Let us consider the up-scaling of the model equations to a relevant geophysical scenario, for example, an oil spill. The focus would be on a continuous oil slick that is being subjected to in-plane shear. The vertical lengths can be scaled with the thickness of the slick, whereas the horizontal lengths can be scaled with the horizontal expanse of the slick. Note that out of all the natural or man-made examples given in this paragraph and mentioned before in this thesis, the case of an oil spill is perhaps the closest to the present research.

The underlying concepts of the present research are applicable to other fields as well. As mentioned previously, the behavior of thin solid elastic membranes is analogous to thin viscous liquid films according to the Stokes-Rayleigh analogy. Knowledge of shear conditions leading to buckling or folding in one could be therefore extended to the other. This observation is relevant to space telescope technology in that elastic membranes, having reflective properties, can potentially replace mirrors and other reflective metal surfaces that are currently employed in orbiting telescopes. Conventional optical and satellite systems are constrained by the limitations of payload size and weight imposed by the launch vehicle. As noted by Wagner (2000), the aperture of the famous Hubble telescope was restricted to 2.4 m by the cargo bay diameter of the space shuttle. It cost approximately 1.6 billion dollars to build, a non-trivial fraction of which was devoted to grinding and finishing. Alternative materials, such as thin elastic films, will not only be lighter to carry as payload, but, due to their flexible nature, can be packed in a compact volume, when compared to conventional reflective materials used today. As pointed out by Wagner (2000), these new materials will be adaptable to various situations, will have larger imaging surfaces, will be controlled with electronically actuated surfaces and will save production cost and time when compared to present technology. However a potentially serious difficulty associated with using pliable elastic materials is the possibility that wrinkles may form in the process of folding or unfolding. Thus it would be helpful to characterize, as in the present work, the conditions that lead to any structural deformation as a result of the forces applied, shear or otherwise.

4.2 Future work

There is ample opportunity for extending the knowledge obtained in the present research. A few ideas are listed below.

The buckling of a thin, viscous film was studied for an axisymmetric geometry here. It would be interesting to study the buckling response of a viscous film, laterally constrained in an asymmetric geometry as shown in figure 4.1. With the variation of the gap width with the cylindrical polar angle, θ, one would potentially expect variations of the wave field morphology, for example the wave amplitude, with θ. A future investigation in this regard would also reveal if the onset of buckling is dictated by the minimum or maximum gap width or some average of the two.

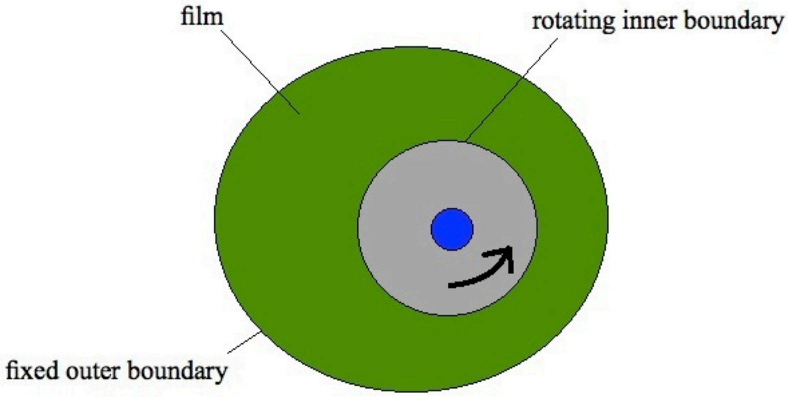

Figure 4.1: Plan view of a thin viscous film subjected to shear in an asymmetric geometry.

Also, the present research employed a Newtonian fluid as the film fluid. Extending this research utilizing a non-Newtonian fluid would highlight the behavior of such films when subjected to in-plane shear. An investigation of this type would be able to better explain isolated observations of previous research groups, such as Benjamin and Mullin (1988), who reported non-Newtonian effects, for the most viscous of their fluids

The wave amplitude measurements in this research were performed with a limited range of independent parameters, for example, a single value for gap width. These measurements can be extended to a wider range of independent parameters like those of the experiments discussed in section 2.1. Depending on the scale of the free surface waves excited in such experiments, it may become necessary to design an optical system that has a finer spatial resolution than the one described in section 2.2.

Moreover, it is believed that the in-plane velocity of the film reaches its maximum value near the rotating inner boundary. As an extension to this study, an attempt could be made to measure the velocity profile across the gap width. In order to make these measurements, the film could be seeded in a similar manner as described in section 2.2. Because the emphasis is then on the velocity of these particles and not the out-of-plane displacement of the film, a stereo PIV technique would ideally be employed. The optical setup could be similar to that shown in figure 2.7.

As a final note, there are a few surprising observations from our experiments whose underlying reasons are unclear. For example, it was observed that for the higher viscosity film, the interval corresponding to a regular wave field was narrower when compared to that of the lower viscosity one. A further investigation into this matter might clarify the underlying cause.

References

Adrian, R.J. (1991). Particle imaging techniques for experimental fluids mechanics. *Annual Review of Fluid Mechanics, 23*, 261 – 304.

Balmforth, N.J., Craster, R. V. and Slim, A.C. (2008). On the buckling of elastic plates. *Quarterly Journal of Mechanics and Applied Mathematics, 61*, 267 - 289.

Benjamin, T.B. and Mullin, T. (1988). Buckling instabilities in layers of viscous liquid subjected to shearing. *Journal of Fluid Mechanics, 195*, 523 - 540.

Bhattacharya, S., Craster, R.V. and Flynn, M.R. (2012). Buckling of a thin viscous film in an axisymmetric geometry. *Submitted to Physics of Fluids, May 2012.*

Biot, M.A. (1961). Theory of folding of stratified viscoelastic media and its implications in tectonics and orogenesis. *Geological Society of America Bulletin, 72(11)*, 1595 - 1620.

Buckmaster, J.D., Nachman, A. and Ting, L. (1975). The buckling and stretching of a viscida. *Journal of Fluid Mechanics, 69(1),* 1-20.

Chakrabarty, P., Lam, C., Hardman, J., Aaronson, J., House, P.H., and Janies, D.A. (2012). SpeciesMap: A web-based application for visualizing the overlap of distributions and pollution events, with a list of fishes put at risk by the 2010 Gulf of Mexico oil spill. *Biodiversity and Conservation*, *21(7),* 1865-1876.

Cobelli, P.J., Pagneux, V., Maurel, A. and Petitjeans, P. (2009). Experimental observations of trapped modes in a water wave channel. *Europhysics Letters, 88,* 20006.

Dave, D. and Ghaly, A.E. (2011). Remediation technologies for marine oil spills: A critical review and comparative analysis. *American Journal of Environmental Sciences, 7*, 424 - 440.

Daviel, J.T. and Rideal, E.K. (1961). Interfacial phenomena. *Academic, New York.*

Drazin, P.G. and Reid, W.H. (1981). Hydrodynamic stability. *Cambridge University Press, Cambridge, U.K.*

Fisher, S. (2010). Most of oil spill remains. *Pollution Engineering 42(8),* 1.

Geminard, J.C., Bernal, R and Melo, F. (2004). Wrinkle formation in axisymmetrically stretched membranes. *European Physics Journal, E 15,* 117 - 126.

Griffiths, R.W. (2000). The dynamics of lava flows. *Annu. Rev. Fluid Mech. 32,* 477 - 518.

Howell, P.D. (1996). Models for thin viscous sheets. *European Journal of Applied Mathematics, 7*, 321–343.

Kamien, R.D. and Liu, A.J. (2007). Why is random close packing reproducible ? *Physical review letters, 99(15)*, 155501.

Kerly, G.I.H. and Erasmus, T. (2005). The management of oiled penguins. *International Oil Spill Conference, 1987, Baltimore, Maryland, USA.*

Kundu, P.K. and Cohen, I.M. (2008). Fluid Mechanics. *Academic Press, Burlington, MA, USA.*

Lagubeau, G., Fontelos, M.A., Josserand, C., Maurel, A., Pagneux, V. and Petitjeans, P. (2010). Flower patterns in drop impact on thin liquid films. *Physical review letters, 105,* 184503.

Lambert, J., Duhon, D. and Peyrefitte, J. (2012). 2010 BP oil spill and the systematic construct of the Gulf Coast shrimp supply chain. *Systematic Practice and Action Research, 25*, 223-240

Moisy, F., Rabaud, M. and Salsac, K. (2009). A synthetic Schlieren method for the measurement of the topography of a liquid interface. *Exp Fluids. 46*, 1021 - 1036.

Ribe, N.M. (2012). All bent out of shape: Buckling of sheared fluid layers. *J. Fluid Mech., 694,* 1 - 4.

Slim, A.C., Balmforth, N.J., Craster, R.V. and Miller, J.C. (2009). Surface wrinkling of a channelized flow. *Proceedings of the Royal Society, 465(2101),* 123 - 142.

Slim, A. C., Teichman, J., and Mahadevan, L. (2012). Buckling of a thin-layer Couette flow. *Journal of Fluid Mechanics, 694*, 5 - 28.

Southwell, R.V and Skan, S.W. (1924). On the stability under shearing forces of a flat elastic strip. *Proceedings of the Royal Society*, *105(733),* 582–607.

Strutt J.W. (Lord Rayleigh). (1945). Theory of Sound - II. *Dover Publications, 313-314, New York.*

Su, Xianyu and Chen, Wenjing. (2001). Fourier transform profilometry: a review. *Optics and Lasers in Engineering. 35,* 263 – 284.

Suleiman, S.M. and Munson, B.R. (1981). Viscous buckling of thin fluid layers. *Physics of Fluids, 24(1),* 0031 - 917/81/01001.

Taylor, G.I. (1969). Instability of jets, threads, and sheets of viscous fluid. *Proceedings of the 12th International Congress of Applied Mechanics*, *Springer-Verlag,* 382 - 388.

Teichman, J.A. (2002). Wrinkling and sagging of viscous sheets. Ph.D. thesis, Massachusetts Institute of Technology.

The International Tank Owners Pollution Federation Limited (ITOPF). Use of skimmers in oil pollution response (2012).
Web:
http://www.itopf.com/informationservices/publications/documents/TIP5UseofSkimmersinOilPollutionResponse.pdf

Wagner, J.W. (2000). Optical metrology of adaptive membrane mirrors. Thesis. Airforce Institute of Technology, Ohio.

Weideman J.A.C. and Reddy S.C (2000). A Matlab differentiation matrix suite. *ACM Transactions on Mathematical Software*, 26, 465 - 519.

Zhou, J., Dupuy, B., Bertozzi, A.L. and Hosoi, A.E. (2005). Theory for shock dynamics in particle-laden thin films. *Physical Review Letters, 94,* 117803.

Appendix A

In tables A.1 and A.2, the variation of m^* and C_p/Ω with the independent parameters is listed. The Reynolds number is less than 2 in all cases. It is defined as follows:

$$\begin{aligned} Re &= V\,D\,/\,\nu \\ &= (R_i\Omega)\,(R_o - R_i)\,/\,\nu \\ &= (\Omega/\nu)\,[R_i\,(R_o - R_i)] \\ &= (\Omega/\nu)\,(R_iR_o)\,\{1 - (R_i/R_o)\} \end{aligned}$$

where V is velocity, ν is the kinematic viscosity, R_i and R_o are the inner and outer radii, respectively, and Ω is the angular speed.

Table A.3 compares the results of experiments having a seeded film (highlighted in blue) with those of a film devoid of seeding particles.

Table A.1: Data table for *m** and C_p/Ω for a film viscosity of 12,500 cS.

Disc Assembly	β = R_i / R_0	Film Thickness h (mm)	Error in h (mm)	Angular Speed Ω (rad/s)	Error in Ω (rad/s)	Wave Count m*	Error in m*	Reynolds Number Re	Relative Speed (C_P/Ω)	Error in C_P/Ω
A	0.497	2.20	0.20	3.51	0.08	24.67	1	1.52	0.64	0.07
	0.497	2.20	0.20	4.08	0.11	22.33	1	1.76	0.57	0.07
	0.497	2.40	0.22	2.92	0.05	25.20	1	1.26	0.58	0.06
	0.497	2.40	0.22	3.05	0.06	25.40	1	1.32	0.60	0.06
	0.497	2.40	0.22	3.18	0.06	25.00	1	1.37	0.62	0.06
	0.497	2.40	0.22	3.43	0.07	24.70	1	1.48	0.59	0.06
	0.497	2.40	0.22	3.72	0.09	23.10	1	1.61	0.62	0.07
	0.497	2.42	0.22	2.76	0.05	26.33	1	1.19	0.65	0.06
A	0.497	3.50	0.32	3.45	0.08	20.10	1	1.49	0.61	0.08
	0.497	3.50	0.32	3.62	0.08	19.00	1	1.56	0.60	0.08
	0.497	3.50	0.32	3.80	0.09	19.20	1	1.64	0.63	0.08
	0.497	3.50	0.32	3.96	0.10	18.00	1	1.71	0.58	0.09
	0.497	3.50	0.32	4.30	0.12	16.80	1	1.86	0.62	0.10
B	0.670	2.83	0.23	1.72	0.02	33.00	1	0.66	0.53	0.05
	0.670	2.83	0.23	1.95	0.02	31.80	1	0.75	0.54	0.05
	0.670	2.83	0.23	2.10	0.03	29.60	1	0.80	0.57	0.05
	0.670	2.83	0.23	2.35	0.04	25.50	1	0.90	0.57	0.06
	0.670	3.07	0.25	2.54	0.04	23.80	1	0.97	0.57	0.07
	0.670	3.07	0.25	2.61	0.04	22.80	1	1.00	0.61	0.07
	0.670	3.07	0.25	2.74	0.05	22.00	1	1.05	0.62	0.07
B	0.670	4.95	0.40	2.80	0.05	18.50	1	1.07	0.58	0.09
	0.670	4.95	0.40	3.05	0.06	17.00	1	1.17	0.61	0.09
	0.670	4.95	0.40	3.15	0.06	17.20	1	1.20	0.61	0.09
	0.670	4.95	0.40	3.32	0.07	16.00	1	1.27	0.64	0.10
	0.670	4.95	0.40	3.45	0.08	15.40	1	1.32	0.60	0.10
C	0.840	2.67	0.20	1.43	0.01	32.00	1	0.33	0.58	0.07
	0.840	2.67	0.20	1.64	0.02	30.50	1	0.38	0.58	0.07
	0.840	2.76	0.20	0.92	0.01	46.20	1	0.21	0.49	0.04
	0.840	2.76	0.20	0.98	0.01	41.00	1	0.23	0.52	0.05
	0.840	2.76	0.20	1.08	0.01	39.00	1	0.25	0.55	0.05
	0.840	2.76	0.20	1.20	0.01	35.20	1	0.28	0.52	0.06
	0.840	2.76	0.20	1.56	0.02	30.80	1	0.36	0.60	0.07
	0.840	2.81	0.21	0.88	0.00	48.00	1	0.20	0.48	0.04

In Table A.1, the error in Ω varies from 0.01 to 0.11 rad/s. From the error analysis formulae (found later in Appendix C), the error in Ω is proportional to Ω^2; thus a wide variation is observed.

Table A.2: Data table for *m** and C_p/Ω for a film viscosity of 30,000 cS.

Disc Assembly	$\beta = R_i / R_0$	Film Thickness h (mm)	Error in h (mm)	Angular Speed Ω (rad/s)	Error in Ω (rad/s)	Wave Count m*	Error in m*	Reynolds Number Re	Relative Speed (C_P/Ω)	Error in C_P/Ω
B	0.670	1.91	0.16	0.78	0.00	45.00	1	0.30	0.45	0.03
	0.670	1.91	0.16	0.82	0.00	44.00	1	0.31	0.48	0.03
	0.670	1.91	0.16	0.84	0.00	41.20	1	0.32	0.46	0.04
	0.670	1.91	0.16	0.88	0.00	41.00	1	0.34	0.52	0.04
	0.670	1.91	0.16	0.92	0.01	38.60	1	0.35	0.55	0.04
	0.670	1.91	0.16	0.99	0.01	38.00	1	0.38	0.51	0.04
B	0.670	2.95	0.24	0.82	0.00	38.00	1	0.31	0.48	0.04
	0.670	2.95	0.24	0.85	0.00	38.20	1	0.32	0.52	0.04
	0.670	2.95	0.24	0.95	0.01	36.00	1	0.36	0.48	0.04
	0.670	2.95	0.24	1.06	0.01	33.20	1	0.41	0.54	0.05
	0.670	2.95	0.24	1.12	0.01	33.00	1	0.43	0.50	0.05
C	0.840	3.05	0.23	0.50	0.00	33.00	1	0.12	0.45	0.04
	0.840	3.05	0.23	0.56	0.00	32.00	1	0.13	0.42	0.04
	0.840	3.05	0.23	0.65	0.00	29.00	1	0.15	0.48	0.05
	0.840	3.05	0.23	0.68	0.00	29.10	1	0.16	0.54	0.05
C	0.840	4.16	0.31	0.57	0.00	28.40	1	0.13	0.48	0.05
	0.840	4.16	0.31	0.64	0.00	28.00	1	0.15	0.50	0.05
	0.840	4.16	0.31	0.68	0.00	28.10	1	0.16	0.52	0.05
	0.840	4.16	0.31	0.74	0.00	27.00	1	0.17	0.46	0.05
	0.840	4.16	0.31	0.77	0.00	26.00	1	0.18	0.50	0.06

Table A.3: Data table for *m** and C_p/Ω showing the comparison between a seeded film and a film without seeding particles.

Disc Assembly	$\beta = R_i / R_0$	Film Thickness h (mm)	Error in h (mm)	Angular Speed Ω (rad/s)	Error in Ω (rad/s)	Wave Count m*	Error in m*	Reynolds Number Re	Relative Speed (C_P/Ω)	Error in C_P/Ω
B	0.670	2.83	0.23	1.72	0.02	33.00	1	0.66	0.53	0.05
	0.670	2.83	0.23	1.95	0.02	31.80	1	0.75	0.54	0.05
	0.670	2.83	0.23	2.10	0.03	29.60	1	0.80	0.57	0.05
	0.670	2.83	0.23	2.35	0.04	25.50	1	0.90	0.57	0.06
	0.670	3.07	0.25	2.54	0.04	23.80	1	0.97	0.57	0.07
	0.670	3.07	0.25	2.61	0.04	22.80	1	1.00	0.61	0.07
	0.670	3.07	0.25	2.74	0.05	22.00	1	1.05	0.62	0.07
	0.670	3.01	0.25	1.83	0.02	30.2	1	0.70	0.51	0.05
	0.670	3.01	0.25	2.05	0.03	29.0	1	0.78	0.55	0.05
	0.670	3.01	0.25	2.45	0.04	23.4	1	0.94	0.56	0.07
	0.670	3.01	0.25	2.48	0.04	22.0	1	0.95	0.52	0.07
	0.670	3.01	0.25	2.65	0.04	21	1	1.01	0.58	0.08
	0.670	3.01	0.25	2.70	0.05	21.6	1	1.03	0.62	0.08
	0.670	3.01	0.25	2.78	0.05	20	1	1.06	0.56	0.08
B	0.670	4.95	0.40	2.80	0.05	18.50	1	1.07	0.58	0.09
	0.670	4.95	0.40	3.05	0.06	17.00	1	1.17	0.61	0.09
	0.670	4.95	0.40	3.15	0.06	17.20	1	1.20	0.61	0.09
	0.670	4.95	0.40	3.32	0.07	16.00	1	1.27	0.64	0.10
	0.670	4.95	0.40	3.45	0.08	15.40	1	1.32	0.60	0.10
	0.670	4.86	0.40	2.91	0.05	19.40	1	1.11	0.56	0.08
	0.670	4.86	0.40	2.98	0.06	19.60	1	1.14	0.60	0.08
	0.670	4.86	0.40	3.15	0.06	17.80	1	1.20	0.58	0.09
	0.670	4.86	0.40	3.22	0.07	16.10	1	1.23	0.61	0.10
	0.670	4.86	0.40	3.24	0.07	16.00	1	1.24	0.64	0.10
	0.670	4.86	0.40	3.41	0.07	14.8	1	1.30	0.62	0.11

Appendix B

The table below presents the data obtained from the wave amplitude experiments. The rows in a shade of blue, correspond to the data points in the region of bistability, i.e. two values of A are listed for each value of Ω.

Note that, for a particular angular speed, multiple composite images are processed. The average value of wave amplitude is shown under the column ‘Wave Amplitude’ whereas the minimum and maximum values of the individual wave amplitudes computed for each composite image are listed under ‘A min’ and ‘A max’, respectively.

Table B.1: Data table for *A*.

Film Viscosity γ (cS)	**Film Thickness h (mm)**	**Error in h (mm)**	**Angular Speed Ω (rad/s)**	**Error in Ω (rad/s)**	***A* min (pixel)**	***A* max (pixel)**	**Wave Amplitude *A* (pixel)**	**Wave Amplitude *A* (mm)**
12500	3.15	0.26	1.90	0.02	8	14	10.8	0.21
12500	3.15	0.26	1.92	0.02	9	15	12.6	0.24
12500	3.15	0.26	1.98	0.02	9	16	12.0	0.2
12500	3.15	0.26	2.10	0.03	8	16	13.0	0.2
12500	3.15	0.26	2.25	0.03	11	29	14.2 and 27.0	0.27 and 0.53
12500	3.15	0.26	2.29	0.03	12	32	15.1 and 31.0	0.29 and 0.59
12500	3.15	0.26	2.31	0.03	27	35	32.1	0.61
12500	3.15	0.26	2.35	0.04	29	34	31.6	0.60
12500	3.15	0.26	2.47	0.04	29	39	34.2	0.65
12500	3.15	0.26	2.54	0.04	32	42	37.8	0.72
12500	3.15	0.26	2.56	0.04	35	43	38.1	0.72
12500	3.15	0.26	2.61	0.04	35	44	37.4	0.71
12500	3.15	0.26	2.72	0.05	34	43	38.4	0.73
12500	3.96	0.32	2.20	0.03	9	16	12.2	0.23
12500	3.96	0.32	2.32	0.03	10	16	14.8	0.28
12500	3.96	0.32	2.36	0.04	12	17	14.4	0.27
12500	3.96	0.32	2.44	0.04	13	34	16.6 and 32.1	0.32 and 0.61
12500	3.96	0.32	2.50	0.04	14	38	17.1 and 36	0.32 and 0.68
12500	3.96	0.32	2.62	0.04	34	43	41.1	0.78
12500	3.96	0.32	2.74	0.05	37	46	43.4	0.82
12500	3.96	0.32	2.78	0.05	38	46	42.2	0.80
12500	3.96	0.32	2.88	0.05	40	50	45.0	0.86
12500	3.96	0.32	2.94	0.06	38	49	45.3	0.86
30000	2.04	0.17	0.76	0.00	10	28	12.2 and 26.4	0.23 and 0.50
30000	2.04	0.17	0.79	0.00	22	30	28.0	0.53
30000	2.04	0.17	0.85	0.00	25	33	27.3	0.52
30000	2.04	0.17	0.88	0.00	28	34	30.0	0.57
30000	2.04	0.17	0.90	0.01	29	33	31.2	0.59
30000	2.04	0.17	0.92	0.01	29	35	31.6	0.60
30000	2.04	0.17	0.95	0.01	30	36	34.0	0.65
30000	3.01	0.25	0.84	0.00	12	34	14.8 and 31.8	0.28 and 0.60
30000	3.01	0.25	0.88	0.00	13	36	14.6 and 33.0	0.28and 0.63
30000	3.01	0.25	0.95	0.01	30	38	35.6	0.68
30000	3.01	0.25	0.98	0.01	33	39	37.1	0.70
30000	3.01	0.25	1.00	0.01	32	39	36.2	0.69
30000	3.01	0.25	1.06	0.01	35	43	39.0	0.74
30000	3.01	0.25	1.09	0.01	37	44	42.8	0.81
30000	3.01	0.25	1.10	0.01	39	45	42.6	0.81

Appendix C

This appendix is dedicated to the error analysis for the film thickness, h, the angular speed, Ω, and the relative speed, C_p/Ω.

Given a function $g = \frac{x}{y}$, the formula applied to find the error Δg is given by

$\Delta g = \frac{x(\Delta y) \ \ + x(\Delta y)}{y^2}$, where Δx and Δy denote, respectively, the error associated with x and y.

From (2.1), $h = \frac{q}{\rho\,\pi(\,R_o^2 - R_i^2)}$

Therefore, $\Delta\, h = \frac{q.\Delta(\,R_o^2 - R_i^2) + (\,R_o^2 - R_i^2).\,\Delta q}{\rho\,\pi(\,R_o^2 - R_i^2)^2} = (\frac{2.\Delta R.h}{R_o(1+\beta^2)}) + (\frac{\Delta q}{\rho\pi {R_o}^2(1+\beta^2)})$,

Where $\Delta\, R = 0.05$ cm and $\Delta\, q = 0.005$g.

From (2.2), $\Omega = \frac{2\ \pi\ f}{n} = \frac{200\,(fps)\pi}{n}$ (since $f = 100$ frames per second)

Therefore, $\Delta\,\Omega = \frac{200\pi\,(\Delta n) + 0}{n^2} = 4\,\frac{200\,\pi}{n^2} = 4\,.\frac{200\,\pi}{n}.\frac{200\,\pi}{n}.\frac{1}{200\,\pi} = 4\,\frac{\Omega^2}{200\,\pi} = \frac{\Omega^2}{50\,\pi}$

Note that in the above expression, $\Delta n = 4$, because n, which is the number of frames taken by the disc assembly to complete one full rotation was determined by multiplying by four the number of frames taken by the disc assembly to rotate by 90^0.

As noted in chapter 2, the relative speed, C_p/Ω, is the same as the ratio between the number of waves crossing a reference point in an image sequence for one full rotation of the disc assembly and the total number of waves, m^*. Hence the error in C_p/Ω is the same as the error in p/m^*, where p is defined as follows

$\Delta(\,p/m^*) = \frac{p(\Delta m^*) + m^*(\Delta p)}{m^{*2}} = \frac{p + m^*}{m^{*2}} = \frac{m^*(Cp/\Omega) + m^*}{m^{*2}} = \frac{(Cp/\Omega)+1}{m^*}$.

Note that in the above equations, Δm^* and Δp are both equal to one. The data tables presented in Appendix A show the errors in Ω and C_p/Ω based on the above error analysis.

Appendix D

Free surface deflection *H*

Writing (1.12) again, the film deflection is given as

$H = f(r)\, e^{\sigma t + im\theta}$ + c.c.

The growth rate being, in principle, complex, σ can be divided into real and imaginary components, i.e.

$\sigma = \sigma_r + i\sigma_i$

Thus, equation (1.12) can be re-written as

$$H = f(r)\, e^{(\sigma_r + i\sigma_i)t + im\theta} + \text{c.c.}$$
$$= f(r)\, e^{\sigma_r t}\, e^{i(\sigma_i t + m\theta)} + \text{c.c.}$$
$$= f(r)\, e^{\sigma_r t}\, e^{im[(\frac{\sigma_i}{m})t + \theta]} + \text{c.c.}$$

In the above expression, $\frac{\sigma_i}{m}$ is the phase speed of the wave field. If σ is, a real number, then $\sigma_i = 0$ and the model cannot therefore predict the phase speed of the waves.

Appendix E

The MATLAB script developed for the wave amplitude measurements is given below.

```
% This is a complete code for wave amp measurements


close all;
clear all;
tic

% ----------------------------------------------------------------

% Specifying path for reading image sequence

s='D:\2012RESEARCH\WAVEAMP\IMAGESEQUENCE\sanjay_test6\Cam_Date=12
0306_Time=195541';
s1=strcat(s,'\B000');
s2=strcat(s,'\B00');
s3=strcat(s,'\B0');
s4=strcat(s,'\B');

% ----------------------------------------------------------------

% Cropping limits

r1=200;
r2=350;
c1=1;
c2=500;

% ----------------------------------------------------------------

% im1 = result of addition of a few images in the "no wave"
% region
% im2 = result of addition of a few images in the "wave" region

im1(1:(r2-r1+1),1:(c2-c1+1))=0;
im2(1:(r2-r1+1),1:(c2-c1+1))=0;

im1=uint16(im1);
im2=uint16(im2);

[row col]=size(im1);

% ----------------------------------------------------------------

% Adding images in "no wave" region
```

```
start_index=200;
stop_index=225;

for i=start_index:stop_index


     if (i<=9)
        s=strcat(s1,mat2str(i),'.im7');
     end

     if ((i>9) && (i<=99))
        s=strcat(s2,mat2str(i),'.im7');
     end


     if ((i>99)  && (i<=999))
        s=strcat(s3,mat2str(i),'.im7');
     end

     if ((i>999) && (i<=9999))
        s=strcat(s4,mat2str(i),'.im7');

     end



    a=readimx(s);
    a1=a.Data;
    a2=fliplr(a1);
    a3=rot90(a2);
    a4=a3(r1:r2,c1:c2);

    % b(:,:,i)=a4;
    im1=im1+a4;

    i

end

thresh1=mean(max(im1))/65535;

im11=imadjust(im1,[0 thresh1],[0 1]);
figure, imshow(im11);


im111=medfilt2(im11);
im1111=im11;

% ---------------------------------------------------------------

% Adding images in "wave" region
```

```
start_index=350;
stop_index=375;
for i=start_index:stop_index


     if (i<=9)
        s=strcat(s1,mat2str(i),'.im7');
     end

     if ((i>9) && (i<=99))
        s=strcat(s2,mat2str(i),'.im7');
     end


     if ((i>99) && (i<=999))
        s=strcat(s3,mat2str(i),'.im7');
     end

     if ((i>999) && (i<=9999))
        s=strcat(s4,mat2str(i),'.im7');

     end




    a=readimx(s);
    a1=a.Data;
    a2=fliplr(a1);
    a3=rot90(a2);
    a4=a3(r1:r2,c1:c2);

    % b(:,:,i)=a4;
    im2=im2+a4;

    i

end

thresh2=mean(max(im2)) / 65535;

im22=imadjust(im2,[0 thresh2],[0 1]);
figure, imshow(im22);


im222=medfilt2(im22);
im2222=im22;

% ----------------------------------------------------------------

% In each of the added images (im1 and im2), top down scan
% approach is applied to each column, moving left to right
% columswise in each iteration of the loop.
```

```
% The intensities are saved in a vector.
% The data (vector) is smoothened and polyfitted.

% Two distinct 'regions' are found in the image: first, around
% the minimum value  of the polyfitted data and the second,
% around the maximum value of the polyfitted data.

% The first, or the upper region, corresponds to the area above
% the laser line where the intensities are low; the second, or
% the lower region, corresponds to the area inside the laser line
% region where the intensities are very high.

% A mean intensity is calculated for both the regions
% Final mean (of the above two means) is also found.
% The location of the final mean is found - row value.

% This row value is the position of the wave crest for that
% column in the image.


wave_crest1(1:col)=0;
wave_crest2(1:col)=0;

row1=1;
row2=row;

row_start=1;
row_end=row;

% total height of image is 200 pixels
% upper / lower region = 70 pixels each
% middle / transition region is 60 pixels (top-down)

for icol=1:col

    y1=im111(:,icol);
    y2=im222(:,icol);
    x1=(1:row)/row;
    x2=(1:row)/row;

    y1=double(y1);
    y2=double(y2);

    y11=smooth(y1);
    y22=smooth(y2);

    y1_f1=polyfit(x1,y11',8);
    y1_f2=polyval(y1_f1,x1);

    y2_f1=polyfit(x2,y22',15);
    y2_f2=polyval(y2_f1,x2);
```

```
if icol==round(col/2)
   figure(77); hold on; box on
   plot(y2,row*x2(end:-1:1),'g-')
   plot(y22,row*x2(end:-1:1),'b--')
   plot(y2_f2,row*x2(end:-1:1),'r-')
   % plot(y1_f2,row*x2(end:-1:1),'g-')
   xlabel('intensity');
   ylabel('image (cropped window) height (pixels)');

   paxo_min1=min(y1_f2);
   paxo_max1=max(y1_f2);
   paxo_min2=min(y2_f2);
   paxo_max2=max(y2_f2);



end


% Finding position of wave crest for im1 (no wave region)

min1=min(y1_f2);
max1=max(y1_f2);
range1=0.2*(max1-min1);
row1=max(find(y1_f2<(min1+range1)));
row2=min(find(y1_f2<(max1-range1)));

upper_avg=mean(y1(1:row1));
lower_avg=mean(y1(row2:end));
avg_intensity1(icol)=(upper_avg+lower_avg)/2;

flag=0;

for irow=row_start:row_end

    if ( (flag==0) && (y1_f2(irow) > avg_intensity1(icol)) )

        wave_crest1(icol)=irow;
        flag=1;

    end


end



% Finding position of wave crest for im2 (wave region)


min2=min(y2_f2);
max2=max(y2_f2);
```

```
    range2=0.2*(max2-min2);
    row1=max(find(y2_f2<(min2+range2)));
    row2=min(find(y2_f2<(max2-range2)));


    upper_avg=mean(y2(1:row1));
    lower_avg=mean(y2(row2:end));
    avg_intensity2(icol)=(upper_avg+lower_avg)/2;

    flag=0;

    for irow=row_start:row_end

        if ( (flag==0) && (y2_f2(irow) > avg_intensity2(icol)) )

            wave_crest2(icol)=irow;
            flag=1;

        end


    end
end

x=1:col;

% ----------------------------------------------------------------

% Filtering the wave crest data

for icol=2:col-1

    if ( wave_crest1(icol-1)-wave_crest1(icol)>30 )
        wave_crest1(icol)=wave_crest1(icol-1);
    end

    if ( wave_crest2(icol-1)-wave_crest2(icol)>30 )
        wave_crest2(icol)=wave_crest2(icol-1);
    end

end

% ----------------------------------------------------------------

% Superimposing the wave crest positions on the original image

for icol=1:col

    im1111(wave_crest1(icol),icol)=65000;
    im2222(wave_crest2(icol),icol)=65000;

end
```

```
figure, imshow(im1111);
figure, imshow(im2222);

% ---------------------------------------------------------------

% Finding wave amp

m1=int32(mean(wave_crest1));
m2=int32(min(wave_crest2));

amp=m1-m2
toc

% End of script
```